Factors for pre-conditioning and post-failure behaviour of submarine landslides in the margins of Ulleung Basin, East Sea (Japan Sea)

Senay Horozal[1*], Jang-Jun Bahk[1], Deniz Cukur[2], Roger Urgeles[3], David M. Buchs[4], Sang Hoon Lee[5], In-Kwon Um[2], Seong-Pil Kim[2]

[1]Chungnam National University, Department of Marine Environmental Science, Daejeon, Korea

[2]Korea Institute of Geoscience and Mineral Resources, Daejeon, Korea

[3]Institut de Ciències del Mar (CISC), Barcelona, Spain

[4]Cardiff University, School of Earth and Environmental Sciences, Cardiff, U.K.

[5]Korea Institute of Ocean Science and Technology, Busan, Korea

*corresponding author

Abstract

Glide planes, the basal surface or failure surface upon which submarine landslides initiate, commonly develop along weak, distinctive stratigraphic horizons but their lithological/mechanical characteristics and genetic mechanisms remain largely unknown. We use 2-D multi-channel seismic reflection data, integrated with multibeam bathymetry and deep drilling data from the Ulleung Basin margins, East (Japan) Sea, to: (1) identify and characterize the nature of glide planes associated with submarine landslides; (2) understand the influence of climate-modulated factors in preconditioning slope failures; and (3) document the post-failure evolution of the landslides. 24 glide planes were identified among 38 submarine slides (SL1 – SL38), which correspond to regionally continuous, positive-polarity high-amplitude seismic reflections. Well-seismic integration support ca. 340 ka – 1,200 ka ages of formation of the major glide planes in the southwestern and western margins of the basin. These glide planes developed at the interface between clay-rich sediment deposited during glacial periods and biogenic diatom-rich sediments deposited during interglacial periods. Physical, mineralogical and geochemical properties determined by density, porosity, gamma-ray, shear strength, X-ray diffraction, and X-ray fluorescence data reveal significant lithological and mechanical changes at the interface between these two lithologies. We therefore infer that these interfaces dictate the position of failure surfaces, with the diatom-rich layers acting as a weak layer. Excess pore pressure in these layers is likely due to initial high-water contents (up to 75%) and high compressibility; this is considered an important pre-condition for failure. In contrast, the glide planes along the northwestern margin of the Ulleung Basin (SL34 – 37) are older (ca. 1,200 ka – 2,140 ka). Seismic data further reveal three distinct contrasting styles of

landslide post-failure behavior throughout the margins: (1) evacuated slide scars with areas of smooth seafloor; (2) slide scars with residual debris consisting of blocky sediments; and (3) slide scars with buried intact sediment blocks in front of the headwalls. Lateral variability of fluid flow, sediment composition, and mechanical properties of basal 'weak' layer(s), or the magnitude of earthquakes may have contributed to forming different types of mass-transport deposits (MTDs). Overall, these results show that landslide formation in the East (Japan) Sea result from a complex climatic, volcanic and tectonic interplay that controlled the formation of weak layers. Some of these layers extend regionally and can be identified and mapped by remote geophysical methods and targeted drilling.

Keywords: Ulleung Basin, East Sea (Japan Sea), submarine landslide, multi-channel seismic reflection data, glide plane, weak layer

1. Introduction

Submarine landslides transport large volumes of sediment to the deep sea (Hampton et al., 1996; Masson et al., 2006). They are one of the principal geologic processes of evolution of the continental margins on both active and passive margins. Submarine landslides can be a significant societal risk as they can generate fatal tsunamis (e.g., the 1929 Grand Banks Slide triggered by an earthquake of M=7.2 in the Northern Atlantic Ocean (Piper et al., 1988, 1999), the 1979 Nice Slide in the Northwestern Mediterranean (Dan et al., 2007), and the 2018 Indonesia landslide-induced tsunami (Takagi et al., 2019)). Understanding how landslides can be preconditioned through the development of "weak layers," how they are triggered, and how they transform into downslope mass movements, is crucial for geohazards mitigation.

Failure surfaces of submarine landslides are often characterized by smooth bedding-parallel surfaces in seismic reflection data where the failure movement is translational (Stow et al., 1996; Baeten et al., 2014; Krastel et al., 2018). These bedding-parallel surfaces are often referred to as "weak layers" because their sediment strength needs to be sufficiently lower than the adjacent units (Locat et al., 2014) for a failure to initiate. Although they are key to understanding why slope failures occur, the nature and age of such layers are poorly documented because they are often destroyed by the landslide (Masson et al., 2010; Locat et al., 2013, 2014) and are usually located too deep for conventional coring techniques (Beaten et al., 2014; Urlaub et al., 2018). Where they have been reached by either deep drilling or long piston cores, they commonly exhibit lithology and physical properties distinct from surrounding sediment layers. Glide planes have been identified within contouritic sediments (e.g., Laberg et al., 2001; Baeten et al., 2014); glacial marine clays with strain-softening behavior (Kvalstad et al., 2005); muddy gas-charged sediments (Lykousis et al., 2009); and high-porosity zones enriched in foraminifera (Sawyer et al., 2009) and (or) diatoms (Meckler et al., 2013; Urlaub et al., 2018).

Changes in climate can modulate margin sedimentation and thus precondition a slope to fail as weak layers consisting of specific sediments can form at specific times in a climate cycle (Urlaub et al.,

2018, 2019; Gatter et al., 2020; Badhani et al., 2020). Examples of submarine landslides inferred to have been preconditioned by climate change include (1) the Cap Blanc Slide Complex, offshore Northwest Africa, where failure surfaces are associated with highly compressible diatom ooze layers formed at the end of glacial periods (Urlaub et al., 2019), (2) the AFEN and Gulf of Lions landslides (Gatter et al., 2020; Badhani et al., 2020) where the failure surface is inferred to be at the interface between hemipelagic to pelagic fine-grained clay-rich sediments and (3) the giant Storegga Slide (off Norway) (Bryn et al., 2003; Laberg and Camerlenghi, 2008; Locat et al., 2014; Beaten et al., 2014), where the interface between thick intervals of plumites and contouritic sediments above is interpreted to have served as the basal glide plane.

The deposits of past submarine landslides imaged in seismic data have diverse surface expressions and deposit architectures (Sawyer et al., 2012; Alves, 2015). Some landslides appear to have moved a short distance from their source area, with much internal stratigraphy preserved (i.e., Ursa Basin landslide, Sawyer and Hodelka, 2016; the Tuaheni landslide, New Zealand, Gross et al., 2018). In other cases, landslides appear to have traveled hundreds of kilometers and the initial stratigraphy is completely remolded (i.e., Grand Banks event, Locat and Lee, 2002). Whether or not the failed material liquefies or remains a cohesive failure that is locally deposited will further influence the stability of the system, as the latter can buttress the slope (Kvalstad et al., 2005; Sawyer et al., 2012). If the headwall of a particular landslide was evacuated completely, the failure could continue to back-step without having to overcome any stabilizing mass at the foot of the headwall. Also, the post-failure behavior of landslides is a critical factor in determining tsunami potential, as fast-moving fluidized failures, such as the 1929 Grand Banks, are potentially more destructive than slow, cohesive failures (Moore and Sawyer, 2016). Documenting the post-failure evolution of the landslides can yield important clues to the flow history, which, in turn, has important implications for assessing slope stability and understanding how possible future failures may behave (Sawyer et al., 2012). Despite many landslide studies along the margins of the Ulleung Basin, East Sea, the factors for landslide preconditioning and post failure behaviour of the landslides remain mostly undocumented.

For this study, we integrate densely-spaced wide-coverage multi-channel seismic reflection data, swath bathymetry, and comprehensive high-resolution deep drilling data along the margins of the UB (Fig. 1B). Our goals are to: (1) Document the character of the glide planes and the internal characteristics of the overlying mass-transport deposits (MTDs) along the margins of the Ulleung Basin, East (Japan) Sea; (2) Elucidate the role of weak layers on slope failures, including the influence of glacial-interglacial cycles on pre-conditioning and triggering of the submarine landslides; and (3) Characterize post-failure styles along the basin margins and determine reasons for different MTD slope run-outs; and (4) Estimate the age of landslide glide planes.

2. Regional Setting

The Ulleung Basin is a back-arc basin in the southwestern East (Japan) Sea (Fig. 1). The basin plain of the UB lies at a water depth of 2,200 m and is generally characterized by smooth seafloor except for a few seamounts (Fig. 1). To the north, the basin is bound by the South Korea Plateau, at water depths of 1,000–1,500 m, which has an irregular seafloor (e.g., Chough et al., 2000; Cukur et al., 2016; 2018). The continental shelf along the western margin of the UB is poorly developed, rarely exceeding 20 km in width, and is characterized by low sedimentation rates due to the absence of terrigenous input from large fluvial systems (Fig. 1B; Chough et al., 2000; Cukur et al., 2016). The N-S trending Hupo Bank forms a major topographic high on the shelf that rises 80 m above the seafloor (Fig. 1B). To the east of the bank, the slope has an average slope angle of 3º but can be as steep as 10º in places. The southern margin, on the other hand, is characterized by a broad shelf (30-150 km wide), an upper slope with a mean angle of 2º, and relatively higher sedimentation rates (Lee et al., 2014). Here, the shelf is typically smooth and gently dipping northwards with the shelf break at water depths between 300 and 400 m.

Thick Neogene strata, uplifted and faulted by inversion and back-arc closure, characterize the southern margin. Since the Late Miocene, siliciclastic sedimentation has become dominant in most parts of the basin (Lee and Suk, 1998; Lee et al., 2001). The latest Neogene-Quaternary sedimentary history of the UB includes two distinct intervals (Lee et al., 2001). During the latest Neogene, margin-wide slope failures, caused by the regional deformation due to the back-arc closure, resulted in widespread MTDs, which were sourced from the upper slope of the southern basin margin. In the second interval, from the Pleistocene to the Present, tectonic activity along the basin margins appears to have slowed and mass-flow deposition in the basin decreased considerably. During the Pleistocene and Holocene, MTD source areas and base-of-slope debris aprons retreated rapidly landward, while turbidite and hemipelagic sedimentation prevailed in the central basin (Lee et al., 2001).

At least 38 major slope failures have occurred during the Late Neogene-Quaternary in the UB (Fig. 1C; Horozal et al., 2018), some having resulted in mass-transport deposits of significant volume (~13 to ~550 km³) of mass-transport deposits (Horozal et al., 2016). Urgeles et al. (2019) showed that submarine landslides with volumes above 10 km³ could have significant tsunamigenic potential. Cukur et al. (2016) showed that landslides on the western UB margin are primarily controlled by the location of faults, suggesting earthquakes as a likely trigger for slope failures. Debris flow deposits on the western margin have run-outs up to ~30 km, but landslides in the southern margin can attain run-outs of ~100 km owing to their larger size (Lee et al., 2013).

The East Sea is connected to the North Pacific and adjacent seas through four shallow and narrow straits (with water depths of 12–140 m). Significant changes in oceanographic conditions have occurred in response to glacio-eustatic sea-level fluctuations, which resulted in a sea-level drop of more than 120 m during the last glacial maximum (Park et al., 2000; Yoo et al., 2017). Tada et al. (1999) suggested that the modulation of the volume and character of the surface water inflow through the Korea Strait associated with glacio-eustatic sea-level changes played a key role in the changes in deep-water

ventilation and surface productivity. Together with the changes in oceanic circulation; surface and bottom water currents (i.e., Tsushima Warm Current, Korea Coastal Currents, and North Korean Cold Current), and surface productivity, variations in the influx of Asian aeolian dust to the East Sea have also been suggested in both orbital and sub-orbital timescales (Irino and Tada, 2002; Nagashima et al., 2007; Bahk et al., 2021).

The East Sea, including the margins of the Ulleung Basin (UB) (Fig. 1A), is highly sensitive to climate perturbations, recorded by centimeter- to decimeter-scale alternations of dark and light layers (Bahk et al., 2000; Tada et al., 2015). The dark layers contain high total organic carbon (TOC) and represent glacial and/or stadial periods of higher surface productivity. The East Sea was nearly disconnected from the global ocean during the eustatic sea-level drops and was in a configuration similar to the present Black Sea. In contrast, the light layers are attributed to enhanced deep-water ventilation during interglacial and/or interstadial periods (Tada et al., 2015). Dark layers are laminated, especially in their lowest parts; and bioturbation is minimal (Watanabe et al. 2007). In addition, Logging-While-Drilling (LWD) (such as gamma-ray and density) logs retrieved from the western slope of the Ulleung Basin (UB) suggest that ratios of terrigenous to biogenic materials were modulated by orbital-scale climate changes at least since 2.6 Ma (Bahk et al., 2016). Therefore, the UB margins provide an ideal setting to investigate the effect of climatic changes on the occurrence of submarine landslides.

3. Datasets and Methods

3.1 Swath bathymetry, seismic reflection, and borehole data

The bathymetric information used for interpretations is based mainly on a grid of ~80 m cell size in the X direction and ~100 m in the Y direction (Fig. 1B). The data were acquired by the Korea Hydrographic and Oceanographic Agency (KHOA) during the multibeam bathymetric survey of the East Sea from 1996 to 1997 (http://www.khoa.go.kr).

The 2-D multichannel seismic reflection data include about 13,000 km of stacked profiles provided by the Korea Institute of Geoscience and Mineral Resources (KIGAM); and about 1,100 km of stacked profiles provided by the Korea National Oil Corporation (KNOC) (Fig. 1B; see Horozal et al., 2016, 2017 and 2018 for details). A high-resolution single-channel sparker seismic profile (~40 km-long) collected by KIGAM on the western slope is also used (see Cukur et al., 2016, for acquisition and processing parameters).

Sedimentary data used in this study were collected from the lower slope of the western basin margin in boreholes UBGH1-1 and UBGH2-1_2 (only logging while drilling - LWD) and UBGH2-1_1 (sedimentary recovery and LWD) during the first and second Ulleung Basin Gas Hydrate Expeditions (UBGH1&2). Data consist of: (1) digital core images and x-radiographs; (2) physical properties (GR, density, sonic, thermal neutron h porosity - TNHP) measured by LWD and multi-sensor core logging (MSCL); (3) sampling for grain-size distribution, moisture and density (MAD) measurements, and X-

ray diffraction (XRD) mineralogy (KIGAM, 2007; Ryu et al., 2012; Horozal et al., 2015); and (4) X-ray fluorescence (XRF) element composition. The sampling interval of LWD well-log data is ~15 cm. The TNHP log from the LWD was filtered with a 10-point moving average. Sediment grain size was measured by a laser particle grain size analyzer (Microtrac S3500) (KIGAM, 2007; Ryu et al., 2012) while X-ray diffraction (XRD) and XRF scanning were performed on the core samples, and the half-split core of the site UBGH2-1_1 (KIGAM, 2011). Mineral compositions including opal-A were also analyzed onshore for selected MAD samples by XRD. In XRD data, a small amount of pyrite and NaCl (<4.4% and <4.1%, respectively) were extracted from the total fraction of the mineral composition, and the rest were normalized to the total volume. XRF analysis of selected elemental compositions was performed using a XRF core scanner (ITRAX) on the archive half cores. Mo- X-ray source was operated at 30-40 kV accelerating voltage and a current of 38-50 mA with 10 s measurement time and 2 cm spatial resolution (Bahk et al., 2016). The XRF scan data used here were filtered with a 5-point moving average after removing abnormal peaks due to cracks near the sediment surface (Bahk et al., 2016). Sedimentary facies were defined based on core X-rays, visual core descriptions, grain size data, and digital images following the lithological descriptions of Bahk et al. (2013).

3.2 Seismic horizon interpretation and definition of glide planes and other regional boundaries

We traced ten prominent seismic horizons representing distinct high-amplitude positive-polarity meaning acoustic impedance increase below the unit boundary or hard kick on the reference seismic reflection profile near the shelf edge, which crosses the Sites UBGH1-1, UBGH2-1_1, and UBGH2-1_2 on the lower slope of the western margin (Fig. 2). The horizons are labeled from H1 to H10 in ascending order. Four sub-horizons, H5.1 to H5.4, are further differentiated between H5 and H6. These sub-horizons might be related to prograding sedimentary units linked with major glacial cycles in the uppermost slope, and with missing seismic layers due to slope failure between H6 and H5 below the scar area of SL22 in the reference profile (Fig. 2). These fourteen horizons are tracked along the basin margin with complementary data from composite profiles tied to the reference profile (Supplementary Fig. S1).

Some of the key seismic horizons that could be traced downslope to the positive-polarity, high-amplitude continuous reflections at the base of MTDs are termed "glide plane" (i.e., H5.2 horizon marked by arrows in figure 2B). Glide planes are tracked between the seismic profiles across the southwestern, western, and northwestern basin margins (Fig. 1C). The glide planes further south of SL13 to SL11 could not be tracked due to poor seismic imaging caused by complex structures (faulting and folding).

3.3 Log-core-seismic integration

Correlation between seismic, core and well log data was performed with the aid of synthetic seismograms using time-depth (t-d) charts (see Bahk et al., 2016) (Fig. 3). The best correlation coefficient in the seismic- to well-tie (~65%) was obtained by slightly re-matching (stretch-squeeze) synthetic seismograms with reflected seismic waves. The synthetic seismogram was created from LWD density and velocity, and a statistically created source wavelet extracted from seismic data. The inferred glide planes, characterized by positive polarity and high amplitude reflectors, correlate well with positive excursions in velocity and density (Fig. 3).

Based on the seismic- to well-tie, the key seismic horizons can be positioned on the GR logs, which were previously correlated by Bahk et al. (2016) with the LR04 global benthic oxygen isotope stack of Lisiecki and Raymo (2005) and assigned with orbitally tuned ages of the LR04 curve (Fig. 4). Regional boundaries (RBs) were also positioned on the GR logs at wells UBGH2_1-1 and 2_1-2 to estimate the timing of deposition of the MTDs. Considering the wavelength (λ) of the seismic data, which is about 32 m (dominant frequency (F) of seismic data around 50 Hz within a frequency band ranging between 10–200 Hz, and assuming an avg. interval velocity of 1600 m/s), the vertical resolution or minimum bed thickness that can be resolved in the seismic profile in figure 4 is estimated to be between 4 to 8 m ($\lambda/8$ to $\lambda/4$) (Widess, 1973; Chopra et al., 2006); and for an average sedimentation rate of about 11.5 cm/kyr (Bahk et al., 2016), the associated age error is estimated to be about $\pm$ 35–70 kyrs.

3.4 Estimating landslide mobility

Prior to failure, the stability of a given slope as determined from a classical limit equilibrium Factor of Safety (FOS) calculation depends on (1) the ratio of shear strength to shear stress in static conditions (Morgenstern and Price, 1965; Morgenstern, 1967); and (2) the earthquake-induced seismic loading simulated as a pseudo-static acceleration of k_e*g amplitude (ten Brink et al., 2009). Ke represents cyclic load of an earthquake represented by a constant horizontal acceleration and g is the gravitational acceleration. In this study, we assume the UB western slope undergoes an acceleration of k_e=0.1, the average estimated value for an earthquake intensity of M_w=5, and a distance of 100 km from the epicenter (e.g., Chough and Lee, 1987; Cukur et al., 2016; 2018).

For this study (see section 5.2), we calculated FOS under undrained conditions and also including overpressure (assuming 50% ($r_u=u_e/(\gamma'z)$ normalized 50% excess pore water pressure) using the static formula of Morgenstern and Price (1965) and pseudo-static formula of ten Brink et al. (2009) for seismic loading to shed insights to submarine landslide mobilities (see Cukur et al., 2016 for details). R_u is normalized pore pressure, u_e is effective pore pressure, γ' is buoyant weigh, and z is overburden depth. FOS static and seismic with overpressure (assuming 50% and 75% normalized excess pore pressures, respectively) were also calculated assuming nomalized shear strengths of $Cu/\sigma'v$ = 0.2 and 0.4 which

are usually limits for normally-consolidated sediments. Cu is the undrained shear strength and $\sigma'v$ is the vertical effective overburden stress.

We also estimated Flow Factor limits from the FOS to be able to discuss potential factors for post-failure behaviour and variant MTD geomorphologies. Sawyer et al. (2012) defined the post-failure mobility based on clay and water content of the failed slurries using a Flow Factor (Ff). The Ff is defined as the ratio of driving stress (τD) to resisting strength (τR) and is the inverse of the FOS. The static driving stress consists of the slope angle, bulk density of the sediments, and thickness of the landslide. Dynamic stresses, if present, (e.g., earthquakes) add to the total τD. The resisting strength is the shear strength of the sediments. Submarine landslide behavior was observed in model laboratory experiments (Sawyer et al., 2012; Moore and Sawyer, 2016), with failure occurring when FOS is less than 1.0. Sawyer et al. (2012) found that the greatest potential to flow is associated with the highest ratio of Ff. As the ratio of τD/τR increases, the driving stress is much greater than the resisting strength, and a fast-moving landslide will occur. Conversely, as Ff approaches 1.0, the resisting strength approaches the driving stress, producing a slow-moving, blocky style of failure. A Ff less than 1.0 indicates that resisting strength is greater than the driving stress, and failure will not occur. Fast-moving, fluidized failures, which are more likely to produce tsunamis, typically originate from disintegrative landslides, such as the Grand Banks (Sawyer et al., 2012), not from slow, cohesive, or creeping type failures such as the Tuaheni Landslide Complex in the Hikurangi margin (i.e., Pecher et al., 2018).

4. Results

4.1 Seismic characteristics of glide planes and MTDs and their inferred ages

Mapping of SL along the study area shows that a group of them share a common glide plane in the western and southwestern margins. These glide planes form the base of chaotic- to transparent-seismic bodies representing MTDs, and are characterized by continuous, slope-conformable, positive-polarity (peak or hard event indicating an increase in acoustic impedance) and generally high-amplitude reflections (Figs. 2 and 3). Seismic horizons tracked between SL14 and SL37 yield age estimations ranging between ca. 130 ka and 2,410 ka (H10 to H1, respectively; Tables 1 and 2, and also Supplementary Table S1). The common glide planes in the southwestern and western basin margins root strata between H6 and H5, having estimated ages of ca. 630 ka and 1,200 ka, respectively. Rare exceptions of glide planes younger than H6 occur for SL31–33 rooted at H8 and H7 with estimated ages of ca. 340 ka and 450 ka, respectively. On the northwestern basin margin, correlated glide planes rooted on reflectors H4 and H2 (ranging from ca. 1.53 Ma to 2.14 Ma), making their estimated ages much older than their southern counterparts (Tables 1 and 2).

4.1.1 Southwestern margin

The southwestern margin of the UB contains ten submarine landslides labeled as from SL14 to SL23 (Fig. 1C). Most of the landslides are rooted on a common strata, H6, the most widespread traceable seismic horizon throughout the entire margin. H6 is a high-amplitude continuous seismic reflection that is conformable to the slope sequence (Fig. 5) and is underlain by well-stratified reflections interpreted as undisturbed slope sediments. H6 has inferred age of ca. 630 ka (Fig. 5 and Table 1). Below buried scarps on the upper slope, the sedimentary units above H6 are characterized by the chaotic- to transparent-seismic reflections of mass-transport deposits (MTD's) (i.e., slides/slumps, debris flow deposits; Fig. 5). These MTDs form wedge-shaped bodies with up to 0.1 s TWT thickness (~80 m, assuming a sediment velocity of 1,600 m/s) and thin gradually downslope.

There is also a slide scarp (~60 m high) downslope of the MTD unit, representing the source of the most recent submarine landslide event, rooted on H10, and multiple buried failure deposits located at the base of the slope (Fig. 5). A triangular-shaped intact sediment block with parallel stratified internal reflections is located immediately below the buried scarp (Fig. 5). Seismic data also displays numerous curved, scoop-like listric faults with indentations at the seafloor (Fig. 5).

The glide planes of SL19, 20, and 21 rooted on H5, H6, and H5.2, respectively, are also characterized by high-amplitude, continuous reflections parallel to the slope stratigraphy (Fig. S2). Below scarps on the upper slope, MTD deposits are characterized by chaotic to transparent seismic facies that form eastward thinning wedges. Numerous faults and seismic chimneys are evident in the seismic reflection profiles (Fig. S2).

4.1.2 Western margin

MBES data from the western basin margin show at least ten submarine landslides (SL24 – SL33; Fig. 1C). The upper slope in this region is characterized by continuous, parallel, medium- to high-amplitude reflections. On the W-E seismic profile in Figure 6, the reflector on which is rooted SL27 (H5.3; ca. 880 ka) displays a high-amplitude continuous reflection. Unlike H6 and H5.4 in the southwestern margin, H5.3 has a much smoother surface without any irregularity. Downslope of the SL27 slide-scar, a wedge-shaped MTD unit (~0.04 s TWT or 30 m thick), comprising chaotic to transparent internal seismic reflections, extends ~1 km downslope. A slump body is also evident downslope of the slide scar. Seismic horizon H8 (ca. 340 ka) overlays the MTD unit giving an approximate age of the drape sediments which also provides a rough indication of the age of slope failure.

As with SL27, SL28 and SL29 are also rooted on reflector H5.3 (Fig. 7A-B). However, in contrast to SL27, the buried scar associated with SL28 was evacuated almost entirely, whereas a portion of landslide debris remains in the headwall scarp of SL29 (Fig. 7A-C).

Seismic data reveal that SL31 is rooted on reflector H7 (ca. 450 ka), which forms a slope-parallel, continuous, high-amplitude reflection (Fig. 8A). The paired MTD unit, characterized by chaotic internal reflections, has a thickness of up to 0.05 s TWT (~40 m) and extends ~2 km downslope. A high-resolution sparker profile traversing SL31 shows the presence of intact sediment blocks characterized by well-stratified internal seismic reflections within the MTD unit (Figs. 8B-C). Individual blocks attached to the glide plane are up to 35 m high and 100 m in length. Where these blocks occur, the modern seafloor becomes hummocky or undulating (Figs. 8B-C). H10, with an estimated age of ca. 130 ka, overlays this MTD unit. The adjacent SL32 and SL33 are rooted on reflector H8 (ca. 340 ka; Fig. S3).

4.1.3 Northwestern margin

MBES data reveal four submarine landslides in the northwestern margin (Fig. 1C). The base of SL35 corresponds to the glide plane H2, a high-amplitude parallel reflection with an inferred age of ca. 2,140 ka (Fig. 9A). Seismic data reveal an anticline in the upper to middle part of the slope; onlapped by seismic horizons of H1 – H4 (Fig. 9A). There is also a major fault between the folded strata on the west and the basin strata to the east. The headwall scar associated with SL35 is located on a steeply dipping (~11°) bedding plane on the east limb of the anticline. Downslope, the MTD unit is composed of chaotic seismic reflections with a blocky top surface.

As with SL35, SL36 glide plane is rooted on reflector H2 (Fig. 9B) but exhibits multiple detachment levels (H3 and H4) towards the toe of the landslide (Fig. 9B). The total thickness of the MTD unit reaches about 75 m (0.1 s TWT) and is composed of blocky or irregular top and bottom surfaces. It extends for at least ~8 km from the headwall scar located at the steeper east limb of the anticline. The youngest glide plane identified below SL37 is H3 (ca. 1.8 Ma) (Table 2).

4.2 Well-logging and lithologic properties of slope sediments and glide planes

4.2.1 Sedimentary facies

The sedimentary facies (Table S2) of the intervals directly above and below the major glide planes H6, H5.4, H5.3, H5.2, H5.1, and H5 are compared in detail for their physical properties measured by Multi-Sensor Core Logger (MSCL) –Whole Round (-WR) and Split (-S), Logging While Drilling (LWD), grain size and texture in figure 10A-B. Sedimentologic changes are typically within half a meter to a meter. We assume the thickest and dominant sedimentation in a zone up to a few meters thick represents the glide plane physical properties. We correlate these horizons with the seismic profiles that have a maximum resolution of about 4 m.

Main sedimentary facies of the major glide planes include bioturbated mud (BM), homogenous

mud (HM), and crudely laminated mud (CLM). Oblique-laminated mud (OLM) and mud-clast mud (MCM) intervals typically overlie the glide planes (Fig. 10; see Horozal et al., 2015 for details). The BM facies are interpreted as hemipelagic sediments formed under well-oxygenated (interglacial and deglacial periods); CLM facies are inferred to have been deposited in poorly-oxygenated water conditions (glacial periods) (Bahk et al., 2000). OLM/MCM facies are interpreted as MTDs derived from the upper slope (i.e., slide/slump, debris flow deposits; Bahk et al., 2016).

The glide plane H6 lying at 108 mbsf coincides with BM facies and is overlain by CLM dominated facies (Fig. 10A; Table S3). The glide plane H5.4 at 129 mbsf is overlain by OLM/MCM facies and underlain by BM facies (Fig. 10A, Table S3). The H5.3 lies at 141 mbsf and coincides with an interval separating a BM facies above and CLM facies below (Fig. 10B). The glide plane of the reference profile (Fig. 3), H5.2 at 149 mbsf, is a boundary separating CLM facies above and BM facies below (Table S3). The H5.1 is at 159 mbsf, comprising BM facies above and CLM facies below (Table S3). H5.1 is at 159 mbsf, which also shows abrupt physical properties changes above.

4.2.2 Well-logging properties of slope sediments and glide planes

The gamma-ray (GR) values in the cored interval where inferred glide planes are identified range between 30 and 120 API (Fig. 10). The bulk density ranges between ~1.5 and 1.8 g/cm^3 and follows similar trends to the GR (Fig. 10). Typically, bulk densities show higher values at the glide planes (e.g., H5.1, H5, H5.2, H5.3, and H6) and lower values immediately above the glide planes (Fig. 10). P-wave velocity converted from sonic-log values (DT) generally ranges between about 1450 and 1650 m/s. The inferred glide planes are characterized by relatively higher P-wave velocities (Fig. 10). Resistivities are typically less than 1.0 ohm-m, while significant resistivity anomalies, reaching ~5.0 ohm-m, occur where there is hydrate accumulation in pore fillings or cracks (Fig. 10). Overall, the inferred glide planes are associated with lower porosities. The lowest porosities (ca. 30%) are recorded within interpreted gas hydrate-bearing zone.

4.2.3 Physical properties of slope sediments and Factor of Safety (FOS)

The slope sediments consist chiefly of silt with a mean grain size of 6.7 phi (ϕ) (Fig. 11). Overall, wet bulk density shows some minor fluctuations in the range between 1.4 – 1.7 g/cm^3. In contrast, the shear strength shows a marked variability down the well and displays a sharp drop at ~105 mbsf coinciding with the zone above the glide plane H6. The shear strength above H6 shows a prominent high peak (~100 kPa) and drops to ca. 30 kPa along the H6. However, the shear strength values below ~30 m are not reliable because the sediments below may have experienced significant deformation during the submarine landslide events and/or removal of in-situ conditions and overburden stress during coring operations. We, therefore, derived the shear strengths for our assessment from the vertical stress (Cu/σ'v)

for 0.2 and 0.4, which is the range for normally consolidated marine sediments. The red dashed line in figure 11 marks the lower limit of shear strength for normal consolidation (Cu/σ'v=0.2); we consider values below 0.2 as dubious. However, the measured shear strength values over the glide plane H6 (at 108 m) are consistent with derived shear strength values for the normally consolidated sediments. Shear strength measurements under the limit of normal consolidation mostly coincide with MTD units shaded in gray (Fig. 11).

The uppermost (<30 m) slope sediments, in which the shear strength values are most reliable (see above), are relatively stable (FOS > 1) under static and seismic conditions (Fig. 11). However, if we introduce 50% overpressure in the stability calculations, the values of $FOS_{\text{static with overpressure}}$ and $FOS_{\text{seismic with overpressure}}$ drop to less than 1.0 at 25 m, coinciding with the location of the glide plane H10. These results suggest that even with a considerable ground acceleration (M_w 5; $k_e = 0.1$), a slope failure is not initiated as FOS_{eq} is over 1.0. Hence, additional factors such as overpressure or a stronger earthquake are necessary to set off landslides at present. Given the lengthy time scale of these strata (2 + million years), it is highly likely that earthquakes much stronger than M~5 affected this area. There are many good examples of historic M>7 intra-plate or back-arc earthquakes (e.g., the AD 1755 Lisbon earthquake (Silva et al., 2021); 1811-1812 New Madrid earthquake (Mueller et al., 2004)). Even if such strong earthquakes only happened every 100,000 years, that would still be 20 events in 2 million years. Hence large events with long recurrence intervals could have impacted our study area. Previous studies from the northwestern margin of the UB also suggest that a minimum of 70% of overpressure would be needed to drop FOS to 1.0 at the proposed failure plane (Cukur et al., 2020). Similarly, in this study, FOS calculated under earthquake loading with an overpressure of 75% using derived shear strengths and overburden stress (Cu/σ'v=0.2) from bulk densities indicates slope instability (Fig. 11), but 50% overpressure for the same parameters results in stability of the slopes ($FOS_{\text{static and eq}} \geq 2.0$).

4.2.4 Mineralogical and elemental compositions

XRD (Fig. 12; KIGAM, 2011) analyses were carried out on sediments at Site UBGH2-1_1 to reveal the mineral composition of slope sediments. The terrigenous (Quartz(Qz) + Albite + K-Feldspar(Fsp)) fraction ranges between 18 and 46% (mean: 33%) and the biogenic (Opal-A + Calcite + Dolomite) fraction ranges between 18 and 65% (mean: 36%), respectively. The clay minerals include muscovite, chlorite, kaolinite, and illite, and the total clay volume of sediments ranges between 16–43%, with an average of 30% (Fig. 12). Lower concentrations of Opal-A and higher concentrations of terrigenous and clay contents correlate well with glaciations and/or lower sea levels and also coincide with the inferred glide planes. MAD and LWD densities and GR consistently increase in these intervals (Fig. 12), whereas porosities decrease. It is striking that major glide planes (i.e., H5, H5.1, H5.2, H5.3, H5.4) occur in sedimentary intervals associated with the least Opal-A (Fig. 12), whereas the sediments

overlying glide planes (weak layers) have the most.

Bahk et al. (2016) used XRF geochemical data (Ti, Ca, and Br) to document compositional changes correlated to LWD logging data. Here we examine the same data to determine compositional changes associated with the inferred glide planes (Fig. 13). The inferred glide planes are commonly associated with low Br/Ti and Ca/Ti values (Fig. 13), which reflect low algal (Br) and carbonate (Ca) productivity relative to the terrigenous (Ti) supply. This observation is consistent with the deposition of glide plane sediments (low Br and Ca) during glacial periods when surface productivity might have reduced significantly.

We made binary diagrams using XRD and LWD log data to (1) document any relationship between the composition of the slope sediments and (2) outline those measures that are within ±4 m depth range of the seismic horizons for calculated seismic resolution thickness (colored points in Fig. 14) to identify if they have distinctive compositions. Binary diagrams for the XRD data (Fig. 14A-C) show a negative correlation between clay versus (vs.) biogenic content (R^2=0.76), Opal-A vs. clay content (R^2=0.46), and terrigenous vs. biogenic sediments (R^2=0.66). These diagrams suggest that the dominant controlling factor in this sequence is biogenic productivity. Although weak (R^2=0.3), there is a positive correlation between GR and density.

Binary diagrams give also some information about sediment composition and physical properties associated with the inferred glide planes within the seismic resolution of 8 meters (colored points in Fig. 14A-D). The sedimentary beds associated with glide planes are mainly concentrated in the end members of the compositional continuum of the sediments (i.e., high clay content, density, GR; Fig. 14A-D). In particular, the beds with the labeled depths in which we picked a seismic to well tie, appear to be compositionally different than the majority of the background sediments (black dots) and are therefore very likely associated with the reflections corresponding to the possible glide planes. These types of binary diagrams are important for recognizing the lithology of possible glide planes even though the resolution from seismic profiles is only 8 meters.

5. Discussion

5.1 Climate controls on the development of weak layers and glide planes

Submarine landslides detach and initiate motion along weak layers or glide planes, and determining the nature and age of these planes is critical to understand landslide occurrences. Using marine oxygen isotopes on benthic foraminifera together with well logs (i.e., GR, density, and p-wave velocity) to determine climatic cycles and mineralogical contents of sediments (e.g., biogenic opal vs clays), it was showed that climatically-induced modulation of the sediment composition occurred on the western slope of the UB since 2.6 Ma, with an increased abundance of terrigenous components relative to biogenic components during interglacial periods (e.g., Tada et al., 1999; Bahk et al., 2016). The high

biogenic opal contents in the East Sea have been attributed to enhanced productivity in a marine environment associated with high sea levels (Kido et al., 2007; Khim et al., 2007). In this study, age estimates derived from seismic- to well-tie and their comparison to marine isotope stages (MIS) suggest that deposition of strata associated with glide planes corresponds to sea level low stands with a vertical seismic error limit of ± 4 m and an age error limit between ±35 kyr (Fig. 15). When the error range is plotted on the LR04 curve, it is evident that the gray bands outlining the age limits of the glide planes (as defined between H8 and H5) still fall into the glacial periods on the southwestern and western margins of the UB (Fig. 15). This suggests that climate modulation leading to variations in the sediment composition was the dominant factor determining the stratigraphic position of glide planes. XRD and XRF sediment analyses also support this correlation because the abundance of terrigenous minerals (i.e., quartz + feldspar + clay) relative to biogenic components (i.e., opal + calcite) increases during interpreted glacial intervals (Figs. 12 and 13).

Although our findings could be regarded as a typical example of the effects of climate change on submarine landslides, other studies have also suggested that climate can precondition the formation of glide planes on a large, global scale. For instance, Gatter et al. (2020) suggest that lithological contrasts (i.e., overlying sandy contouritic sediments and softer underlying mud-rich sediments) due to changes from cold and uniform to warm and variable climatic conditions played a key role in the location of failure planes in the ~2.8 k.y.-old AFEN slide offshore of the Faroe Islands in the North Atlantic. Similarly, Badhani et al. (2020) suggest that lithological heterogeneity (i.e., clay rich material contrasting with the overlying turbidite deposits) caused by climatic changes is a key to the localization of seafloor instability in the Gulf of Lion in the Mediterranean during the LGM. Source areas for submarine landslides offshore NW Africa in the Central Atlantic have been associated with weak layers containing abundant marine diatoms (siliceous microfossils) overlain by clay-rich interbeds deposited at the end of glacial periods (Tiedemann, 1991; Meckler et al., 2013; Urlaub et al., 2018). Our results from the relatively restricted East Sea Basin further outline that climatic preconditioning of submarine landslides was a common process during Pliocene to Quaternary glacial cycles.

5.2 Sedimentological and geophysical characteristics of the glide planes

The identification and characterization of glide planes and weak layers are important to understand the mass wasting processes and to correctly perform geohazard assessments (L'Heureux et al., 2012; Baeten et al., 2014; Badhani et al., 2020). In the study area, MCS data reveal that the glide planes form positive polarity, high-amplitude continuous reflections that separate chaotic reflections of highly deformed MTD units from the underlying undisturbed slope-parallel sediments (Figs. 5-9). The strata-parallel or planar glide surfaces in the UB slopes further suggest the dominance of translational slides over rotational failures (Baeten et al., 2014; Llopart et al., 2015; Krastel et al., 2018). This behavior is similar to that of sediments mobilized along bedding planes containing discrete weak layers (Hampton

and Lee, 1996; Harders et al., 2010). Seismic correlation in the southwestern and western margins of the UB further reveals that a single glide plane is commonly shared by small (<50 km wide) clusters of landslides (Table 2). This observation strongly suggests that landslides initiated along weak surfaces and were limited by the number and distribution of the weak layers above the glide planes (Figs. 5-9). We discuss below key geophysical and sedimentological characteristics of the planes, which could be used in the future to identify potential (yet-inactivated) failure surfaces in the East Sea using geophysical data (e.g., seismic reflection, LWD density, and GR log), with or without sediment coring.

As already discussed above, the terrigenous (clay-rich) sediments in the East Sea deposited during glacial (low stand) periods, while biogenic opal-rich sedimentary intervals developed during interglacial (high stand) periods (Bahk et al., 2016; Tada et al., 1992, 1999 and 2018). New seismic and core integration provides important constraints on the composition of the glide planes, suggesting that they are associated with high density and velocity that correspond to clay-rich layers deposited during glacial periods (Figs. 3, 12, and 14, and previous section). In the study area, clay-rich layers produce a strong positive reflection in seismic reflection profiles (Figs. 3, 7 and 8). In contrast, the sedimentary beds of low density and velocity, high porosity, and high biogenic opal content that deposited during the interglacial periods seem preferentially associated with high amplitude, negative-polarity reflections overlying the inferred glide planes (Figs. 3, 7, and 8). This (apparently) simple correlation between seismic and core data could prove useful to identify landslides in the making in East Sea sediments, as is also further discussed below using well log and core data.

The cyclic variations in the LWD density and GR logs at Site UBGH2-1_1 cannot be attributed to changes in grain size (sand to mud ratio) because the recovered sediments are dominated by fine silt (90%) throughout the drilled interval with uniform mean grain sizes mostly between 5.8 and 7.24 ϕ (Bahk et al., 2016). Although the sediment size is remarkably uniform (Fig. 11), the sediment mineralogy shows a higher variability in the XRD data (Fig. 12), in particular total biogenic (siliceous) vs. total terrigenous (feldspar + quartz + clay) contents. Major glide planes correlated to the XRD data correspond to interfaces between the clay-rich terrigenous and opal-rich biogenic sediments, which are also reflected by distinct changes in porosity and other aforementioned physical properties (Figs. 10 and 11). In biosiliceous sediments, the GR and density values decrease as diatom content increases (Tada et al., 2018) because diatom frustules have high internal porosity (at low overburden stresses at least) and biogenic opal and organic matters are non-radioactive (Bahk et al., 2016). As shown in the well-log and core sample data, the diatomaceous opal-rich intervals are characterized by high porosity, high water content, low density, and high Br/Ti geochemical ratio in the inferred interglacial periods (H5.2 and H5.1) that typically occur in intervals just above the glide planes. In contrast, the low stand clay-rich intervals deposited during glacial intervals (Figs. 10A-B and 13) are characterized by low porosity (and likely low permeability), lower water content and high density (Figs. 10A-B), and high Ti content (Fig. 11). An important implication of preceding observations is that high water content could elevate pore water pressure within diatom-rich, weak layers, thus promoting slope failures, e.g., following an external

trigger such as an earthquake, or an internal trigger such as pore pressure buildup in response to sediment burial and loading.

Although relative clay abundance could be regarded as the dominant factor controlling the formation of landslides in the study area, diatoms are also known to significantly influence the geotechnical properties of sediments, even in minor amounts. Water content, permeability, compressibility, and friction angle all increase with the abundance of diatoms in the sediment (Bryant et al. 1981, Tanaka and Locat, 1999; Wiemer et al., 2017). In biogenic opal-rich layers, additional porosity is provided by unfilled individual diatom frustules. These porous, diatom-rich layers could generate excess drainage of pore fluids during their burial due to their high initial water content and compressibility (Tanaka and Locat, 1999; Urlaub et al., 2018). Because of the relatively low porosity (<50%) and low permeability of the overlying clayey deposits, excess pore pressure can build up at the boundary between diatom-rich and clay-rich lithologies, ultimately forming weak layers. In other words, it is to be expected that high clay and diatom abundances in discrete sediment layers control *together* landslide formation in the East Sea.

To better understand the role of pore pressure, we calculated the FOS values using derived undrained shear strengths (assuming $Cu/\sigma'v=0.2$ as the lower limit) of normally-consolidated sediments. Slope sediments are stable under static conditions with excess pore pressures of 50% to 75%. Even if a seismic acceleration coefficient is applied (i.e., pink squares in figure 11), the required excess pore pressure would need to be 75% or more. Reaching such value in the study area is geologically feasible given that pore water saturation can exceed 75% in the opal-rich intervals that are typically associated with the glide planes (Fig. 12). These observations are consistent with our inference that the slope failures in the southwestern and western margins of the UB initiated along seismically-identifiable, lithological interfaces that formed during cyclical transition from warm (interglacial) to cold (glacial) climatic conditions.

5.3 Timing of formation of the submarine landslides

The timing of formation of the studied submarine landslides was estimated using biostratigraphical and tephrochronological constraints from previous drill sites (e.g., Bahk et al., 2016) and our regional seismic correlations. Specifically, an age of ca. 1.2 Ma is inferred for the seismic horizon H5, the youngest age estimation for the glide plane of SL34 (Tables 1 and 2). For SL35, 36, and 37, the estimated ages of the glide planes are ca. 2.14 Ma, 1.56 Ma, and 1.88 Ma, respectively (Table 2), coinciding with the end of glacial (H4) and interglacial epochs (H3 and H2). Hence, glide planes on the northwest UB margin appear to be much older (ca. early Pleistocene - late Pliocene) than their counterparts on the western and southwestern basin margins (< ca. 1.2 Ma). This trend correlates with regional changes in sedimentation rates, which seem to be low within the uppermost slope sediments on

the northwestern slope (approximately 3 cm/kyr; Cukur et al., 2020) compared to the rest of the study area (approximately 10 cm/kyr; Cukur et al., 2016.); the age of deposition of the uppermost slope sediments in the northern area was estimated to be more than ca. 1.2 Ma just a few tens of meters below the seafloor (Fig. 9B). In addition, the age of horizon H4 matches well with the age data from the DH-1 hole (Fig. 9B), where a tephra (volcanic ash) layer at subsurface depths of 20.1 to 20.5 m yielded a ca. 1.48 Ma K/Ar date (Kwon et al., 2009). Finally, the Brunhes-Matuyama boundary that represent the Earth's latest magnetic field reversal event at ca. 778 ka was identified based on paleo-magnetic data at 17.5 mbsf in this hole (Lee et al., 2013). Overall, these observations reveal that the ages of the strata where glide planes are rooted become older on the northwest slope of the UB, with ages from about 1.2 to 2.14 Ma (green dashed lines; Fig. 15). Possibly lower sedimentation rates in the northern area could be due to local uplift and/or bottom current erosion.

A minimum age of landslide formation can be constrained based on the age of seismic reflectors directly on top of associated MTDs, which represent sediments deposited after failure (e.g., Urlaub et al., 2019). Applying this approach and our preceding age interpretations, we find that the failure events in the western UB occurred between ca. 130 ka and 1.25 Ma (MTD U6-1A – U2-1A; Fig. 4). These ages are consistent with the age models given in Cukur et al. (2016) based on a similar integrative approach of seismic data and core sediment ages. The established age model by Cukur et al. (2016) from the western slope of the UB indicates that the MTD unit that are underlain by hemipelagic sediment is older than 97. 4 ka. However, they are significantly younger than the age of the glide planes on the northwest slope of the UB (ca. 1.2 to 2.14 Ma, see above). Despite obvious regional changes in the timing of landslide formation, the relatively limited level of detail of sedimentation ages in the study area does hampers determining if cyclical climatic conditions in the East Sea (e.g., as discussed in Section 5.3), regional tectonic events (e.g., Lee et al., 2001; Cukur et al., 2016), and/or volcanism (e.g., Shiihara et al., 2013; Lim et al. 2015), played a direct role in the timing of formation of these landslides.

5.4 Contrasting post-failure styles of submarine landslides

Submarine landslides show contrasting failure styles along the southwestern, western, and northwestern margins (Figs. 5-9). The majority of failures show wedge-shaped MTD units immediately below headwall scarps, indicating that some slid material remained on the slope (e.g., Figs. 5 and 6). In contrast, some landslides on the mid-western slope show complete removal of slid material within the headwall area (i.e., SL28; Fig. 7A). The absence of MTDs may suggest that the slid material disintegrated downslope, possibly evolving into turbidity currents.

The differences in post-failure styles of the landslides may result from their sediment compositions and mechanical properties, slope gradients, and trigger mechanisms (Yang et al., 2006; Casalbore et al., 2016; Sawyer et al., 2012, Moore and Sawyer, 2016). Sawyer et al. (2012), based on

mudflow experiments and other early studies (e.g., Elverhøi et al, 2000; De Blasio et al., 2004, 2006; Issler et al., 2005; Locat and Lee, 2005; Jeong, 2010), showed that water and clay-content control the dynamic post-failure behavior of submarine landslides. They demonstrated that sediments with low water contents and/or high proportions of clay-sized grains (~35 %) produce blocky slides found next to the scars, whereas those with high water contents and/or coarse to high silt-sized grains rapidly disintegrate.

Despite a silt-dominant grain size (Fig. 11), XRD data from the southwestern basin margin indicate that slope sediments contain considerable amounts of clay minerals (mean value of 30%; Fig. 12). This relatively large clay component is consistent with the presence of relatively cohesive landslide deposits with short run-out distances (Figs. 5 and 6; see also supplementary figures 2 and 3).

It is not well-understood how grain size and water content interact to affect landslide post-failure behavior. Sediment with ~35% clay fraction can behave as a fast-moving turbidity current or a slow-moving slump simply by reducing the initial water content (see also Jeong et al., 2022). Sediment with a given water content can have significantly different dynamic behaviors by changing the ratio of silt to clay fractions (Sawyer et al., 2012). Based on these observations, blocky deposits (Figs. 5, 6, and 9, S2 and S3) moving relatively short distances from a source region might be attributed to a relatively low flow factor. In contrast, fully evacuated (i.e., SL 28; Fig. 7A) or very thin (SL29; Fig. 7B) landslide deposits may be due to increased water (and related low consolidation) and/or reduced clay content. In this type of failure, the landside deposit is typically thin and tabular, generating a co-genetic turbidity current (Sawyer et al., 2012).

There is no correlation between slope gradients and the development of arrested vs. evacuated MTDs on the UB margins. The gradients of the uppermost slopes, where the headwalls of scars form, are relatively constant throughout the study area. In the southwest (SL14 – 23) where the arrested slid blocks are common, slopes range from 1.5–6º with an average of 3.7º. On the western margin (SL24 – 33), where arrested sediments are thinner or absent, slopes range between 2.7° and 4.5º with an average of 3.4º. On the northwestern margin (SL34 – 36), where landslides deposits are blocky, the slope gradients in the source area range between 1.2 and 3.5º with an average of 2.4º (Horozal et al., 2018). Hence unlike the other landslide-prone continental margins, for instance the eastern Canadian margin (Piper et al., 2012) and the Cascadia margin (Riedel et al., 2018), the regional slope gradient does not influence the type of landslides whether they break up and accelerate as a debris flow or turbidity currents or whether they come to rest near their source.

The different characteristics of landslides (blocky vs disintegrative) may be related to the depth of the weak layer on which the landslide originated. If the weak layer on the upper slope occurs relatively deep (Table 2) and extends into the consolidated strata, the sediments would then remain relatively cohesive not being able to form turbidies. Stronger or consolidated sediments are more likely to remain intact during a slope failure and produce a blocky MTD such as those observed in the Oregon continental

margin (McAdoo and Watts, 2004; Lenz and Sawyer, 2021), offshore Papua New Guinea (Tappin et al., 2002), and offshore Southern California (Watts, 2004). In contrast, the weak layers that occur shallower in the sedimentary sequence would even mobilize cohesive sediments, and this might be the reason why they are characterized by more extensive landsliding. The presence of weak layers (i.e., sand and silt turbidities) in shallow strata could readily shear during earthquake loading and downslope movement resulting in large retrogressive failures of the surficial sediments (Piper et al., 2012).

Contrasts in landslide development and deposit morphology could also be due to variations in the amount of entrapped fluids in sediments along the strike of the basin margin. With significant variation, in the amount of these entrapped fluids, changes in slope angle, the magnitude of earthquake trigger, or sediment characteristics would not be required to explain changes in landslide behavior. Seismic data show extensive evidence of fluids adjacent to the landslides, indicated by the presence of seismic chimneys and enhanced reflections below the bottom simulating reflectors (BSRs) (Fig. 2). These fluids may have been transported upward along faults or other pathways (Fig. 2).

5.4.1 Internal slide-blocks of MTDs

We document triangle blocks or pinnacles (intact sediment ridges or blocks with undisturbed continuous seismic reflections) in MTD units (Figs. 5, 8B, and S2B), characteristic of sediment failure into coherent blocks displaced downslope along a planar glide plane (e.g., Micallef et al., 2007; Bull et al., 2009; Sawyer et al., 2009; Baeten et al., 2013; Kvalstad et al., 2015; Normandeau et al., 2019). The seismic facies between internal blocks are chaotic, suggesting a highly deformed and fractured mass (Fig. 8B) (Baeten et al., 2013). These triangular blocks or pinnacles are still attached to the underlying glide plane, and have not been rotated or overturned (Figs. 5 and 8B), despite extensional dilation seems likely.

A similar phenomena is observed in the Ursa Basin, Gulf of Mexico (Sawyer et al., 2009), where the basal layer of MTDs (glide planes) is a foraminifera-rich clay layer, and only minimal sliding occurred along this surface before all movement ceased (Sawyer and Hodelka, 2016). Sawyer and Hodelka (2016) postulated that as the landslide initiated and shearing continued, foraminifera may have caused the clay to dilate, reducing pore pressure and thereby arresting the movement. We similarly suggest that slope sediments, rich in biogenic opal and clay (Figs. 12 and 13), played an important role in both initiating and arresting stages of the UB slope failures.

Based on outcrops in SE Crete and Spain, Alves (2015) suggested that clay in the matrix of blocks transported *en-masse* contributed to maintaining their internal cohesion when transported downslope. The XRD analysis in the UB shows higher clay mineral content of slope sediments, reaching up to 45%; Fig. 12). It is possible that relatively high clay contents (>30%, Fig. 12) could control the post-failure, cohesive blocky behavior of the sediments in the southwestern and western slopes in the UB. It is also

possible that here the slope angle (< 3°) and release energy were not big enough to allow further downslope sliding. The observation of slide blocks in the area definitely shows that the sediments were cohesive enough relative to the slope so that they did not entirely disaggregate when they started to glide.

6. Conclusions

- By combining multichannel seismic reflection data, multibeam bathymetry, core and logging data from deep drill cores, we identified and characterized glide planes upon which a large number of submarine landslides have occurred in the Ulleung Basin margins.

- The basal surface of landslides (or glide planes) is rooted on a high-amplitude continuous reflection that is regionally mappable and parallel to slope stratification. This suggests that submarine landsliding in the southwestern, western, and northwestern margins of the UB are translational and stratigraphically controlled.

- The major glide planes for submarine landslides are rooted on strata yielding ages ranging between ca. 340 ka to 1.2 Ma (H8 and H5, respectively) in the southwestern and western margins. These planes correspond to sediments deposited during glacial periods and sea-level low stands. The H6 reflector is the glide plane of slides SL14 to SL18 in the southwestern margin. H6 yields an age of ca. 630 ka, when the sea level was the lowest (~120 m lower than the Present). In contrast, the geological ages of submarine landslides are older on the northwestern margin of the basin, ranging between ca. 1.53 Ma and 2.14 Ma (H4 and H2, respectively).

- The seismic-to-core correlation suggests that the slope failures preferentially occurred along diatom-rich sediments that deposited cyclically in the Quaternary during inter-glacial periods and sea level highstands. High initial porosity of these layers led to excess pore pressure during burial, ultimately promoting slope failures. Therefore, long-term climatic modulations exerted a first-order control on slope stability through variations in sediment composition.

- Three contrasting styles of post-failure behavior are observed along the southwestern, western, and northwestern basin margins; (1) landslides with complete evacuation of the slide area; (2) landslides with a cohesive failure style where a significant part of the failed material remains on the source area and partially buttresses the failure scar; and (3) landslides with intact sediment blocks in front of the headwalls. The contrast in post-failure behavior of these landslides can be attributed to variations in sediment clay and/or water contents.
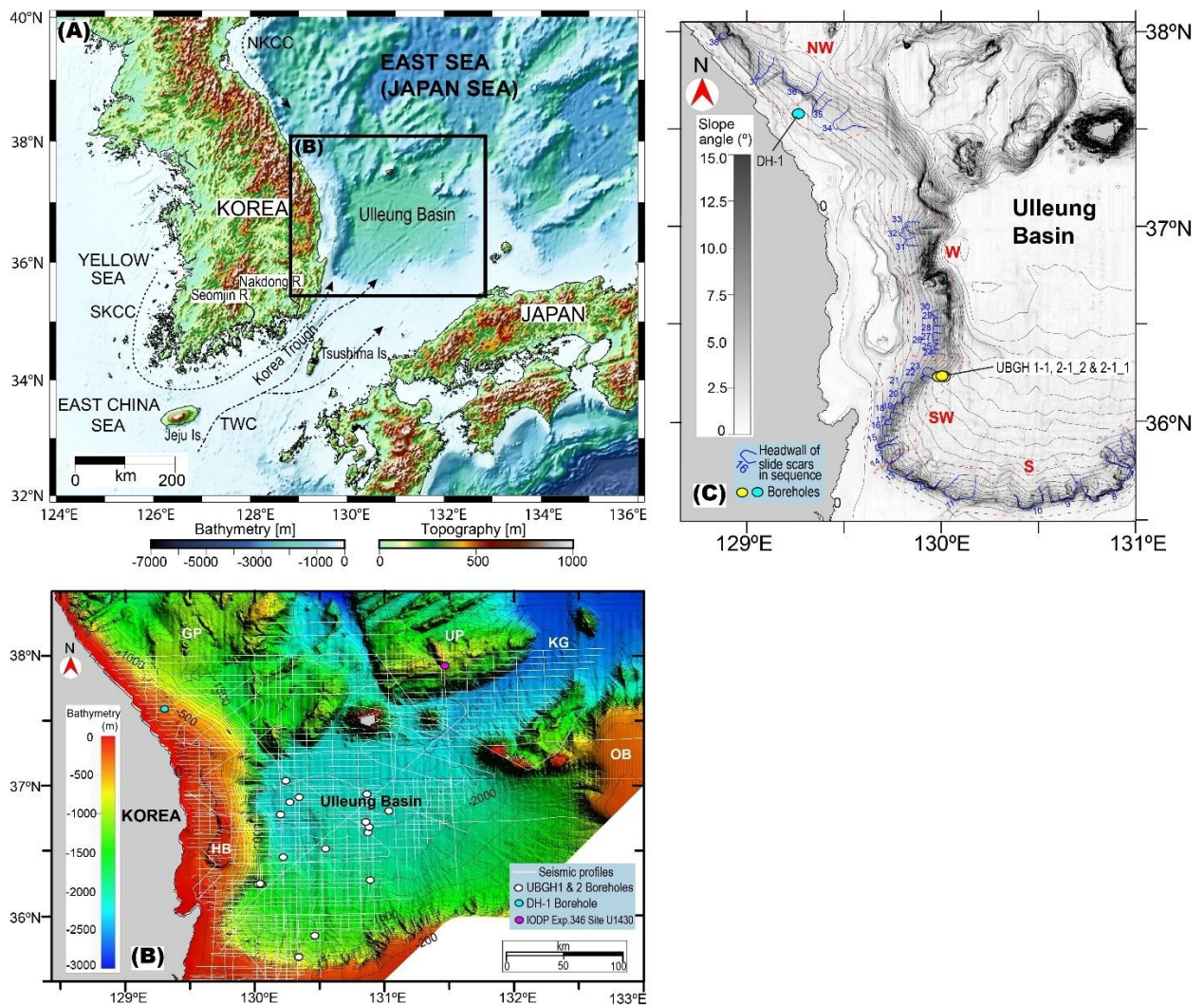
Data availability statement

Supporting of the data were provided by the Korea Institute of Geoscience and Mineral Resources (KIGAM) under confidential status and the restrictions do not allow open sharing of the proprietary data used in this research. The data can be available upon reasonable request made to the authors with permission from the KIGAM.
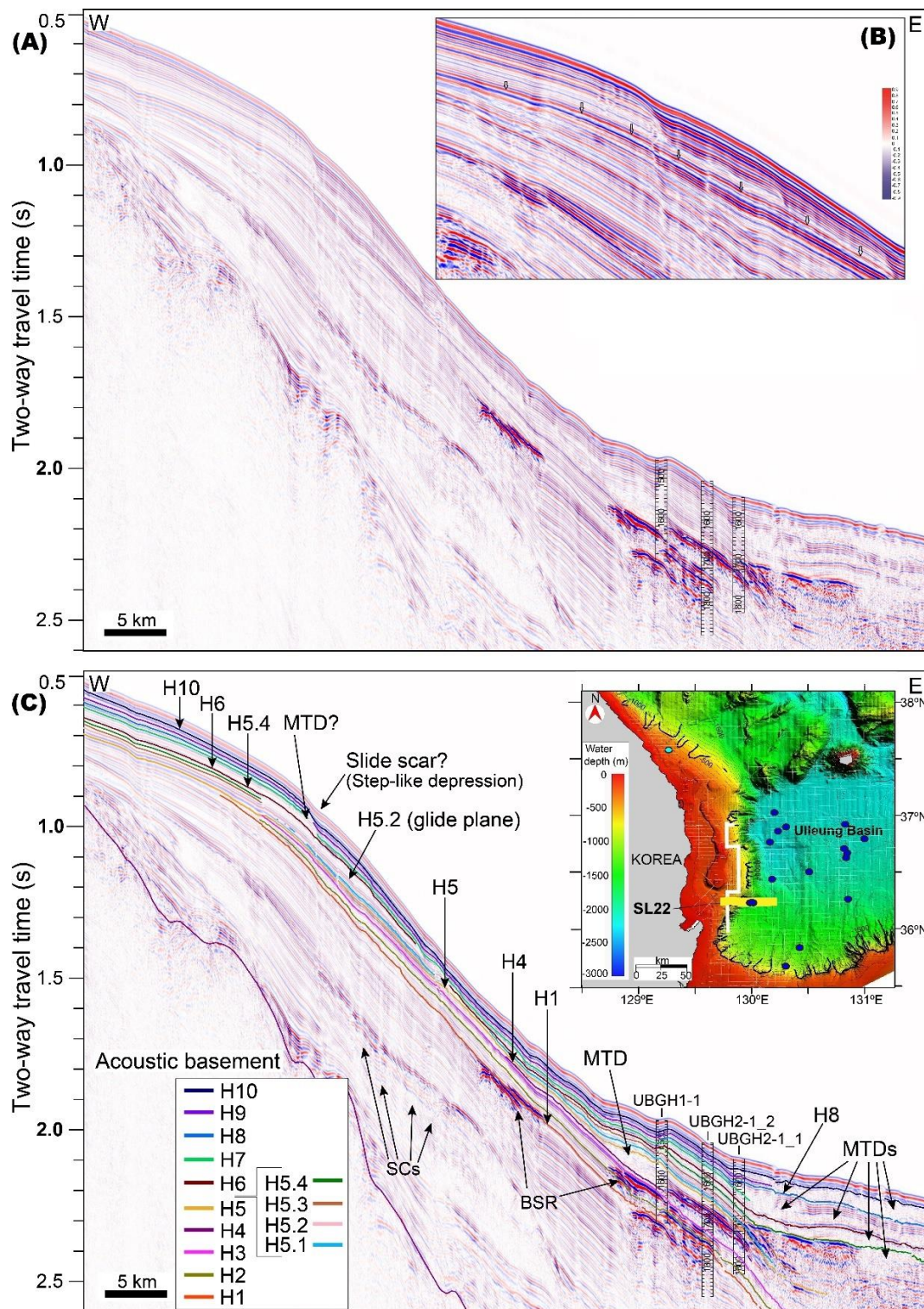
Figures

Figure 1. (A) Index map showing topography and bathymetry of the East Sea and its surroundings. *SKCC*= South Korea Coastal Currents; *TWC*= Tsushima Warm Current; NKCC= North Korean Cold Current. **(B)** Multibeam echosounder bathymetry with location of seismic reflection profiles (white lines) and boreholes in the Ulleung Basin, East Sea. *GP*= Gangwon Plateau or previously Western South Korea (*WSKP*); *UP*= Ulleung Plateau or previously Eastern South Korea (*ESKP*); *KG*= Korea Gap or previously Ulleung Intraplain Gap *(UIG)*; *HP*= Hupo Bank; *OB*= Oki Bank. **(C)** Slope gradient map of the UB showing the headwalls of submarine landslide scarps (designated by numbers) along the UB margins (see Horozal et al., 2018, for details). Submarine landslides (SLs) examined in this study are divided into three groups based on their geographic location, SL14 – 23: southwest (SW), SL24 – 33: west (W), and SL34 – 38: northwest, (NW).
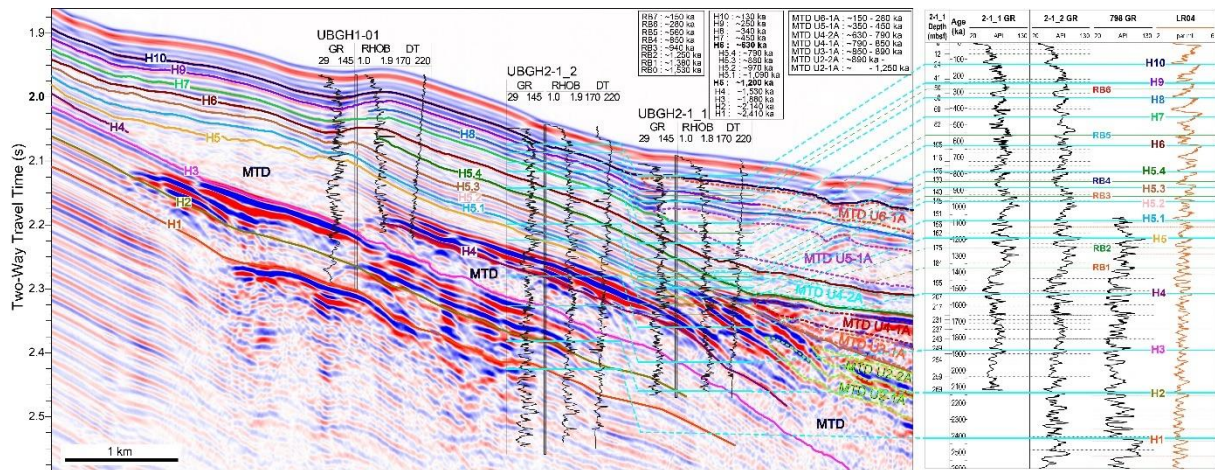
Figure 2. (A) Uninterpreted E-W-trending reference seismic profile from the western slope showing the locations of three boreholes UBGH 1-01, 2-1_1, and 2-1_2. **(B)** Close-up seismic profile highlighting the high amplitude positive polarity seismic reflection (marked by arrows) corresponding to the glide plane of the SL22. **(C)** Interpreted seismic profile of Fig. 2(A) showing stacked mass transport deposits (MTDs) at the base of the slope, and prominent high-amplitude reflections interpreted as BSRs and associated gas/fluid structures, i.e., seismic chimneys (SCs). 10 main (H10– H1) and 4 sub-horizons (H5.4–5.1) are tracked throughout the profile. The yellow bold line in the index map represents the location of the profile shown in figure 2A-C; the white line denotes the location of the N-S arbitrary line that helped track the seismic horizons throughout the margin (see Fig. S1 for the arbitrary seismic profile).
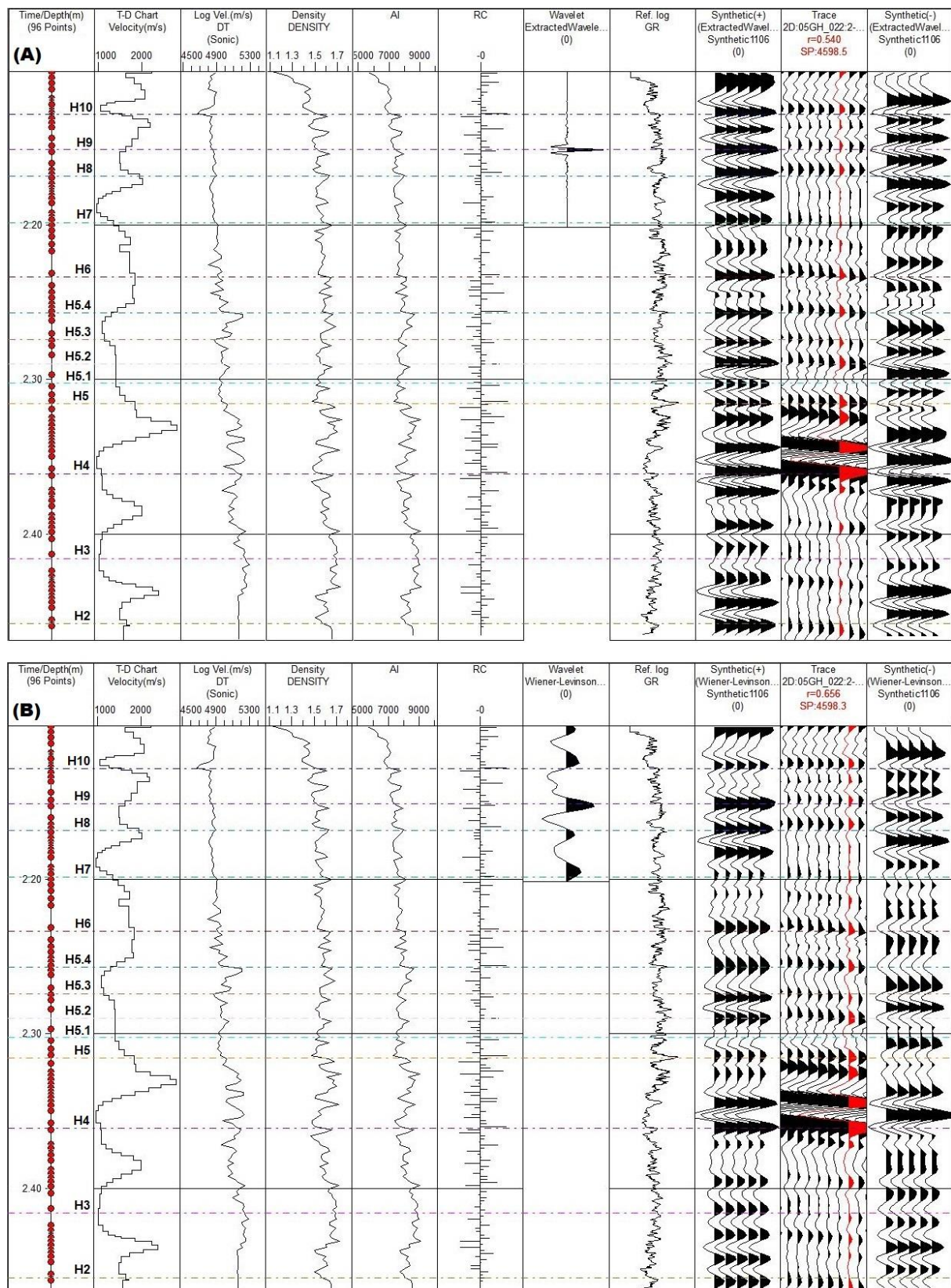
Figure 3. Final synthetic seismogram from which a time-depth (t-d) relationship for well 2-1_1 was established. The synthetic seismograms show a correlation ratio of ~0.66. Note that the inferred glide planes (dashed lines) correlate well with positive excursions in velocity and density.

Horozal et al. (2023) preprint reviewed version - p.24

https://doi.org/10.1016/j.margeo.2022.106956

Figure 4. Close-up seismic profile of figure 2 showing the seismic-to well tie of three boreholes (UBGH1-1, UBGH2-1_1, and 2-1_2). Superimposed on the seismic profile are gamma-ray (GR), density (RHOB), and sonic (DT) log measurements. Curves on the right panel represent GR-logs in age scale taken from the drilling sites UBGH 2-1_1 and 2-1_2 and ODP 798 (black curves), which was correlated (Bahk et al., 2016) with the LR04 marine isotopic stack (orange curves) from Lisiecki and Raymo (2005). RB= regional boundaries; MTD U= mass transport unit.
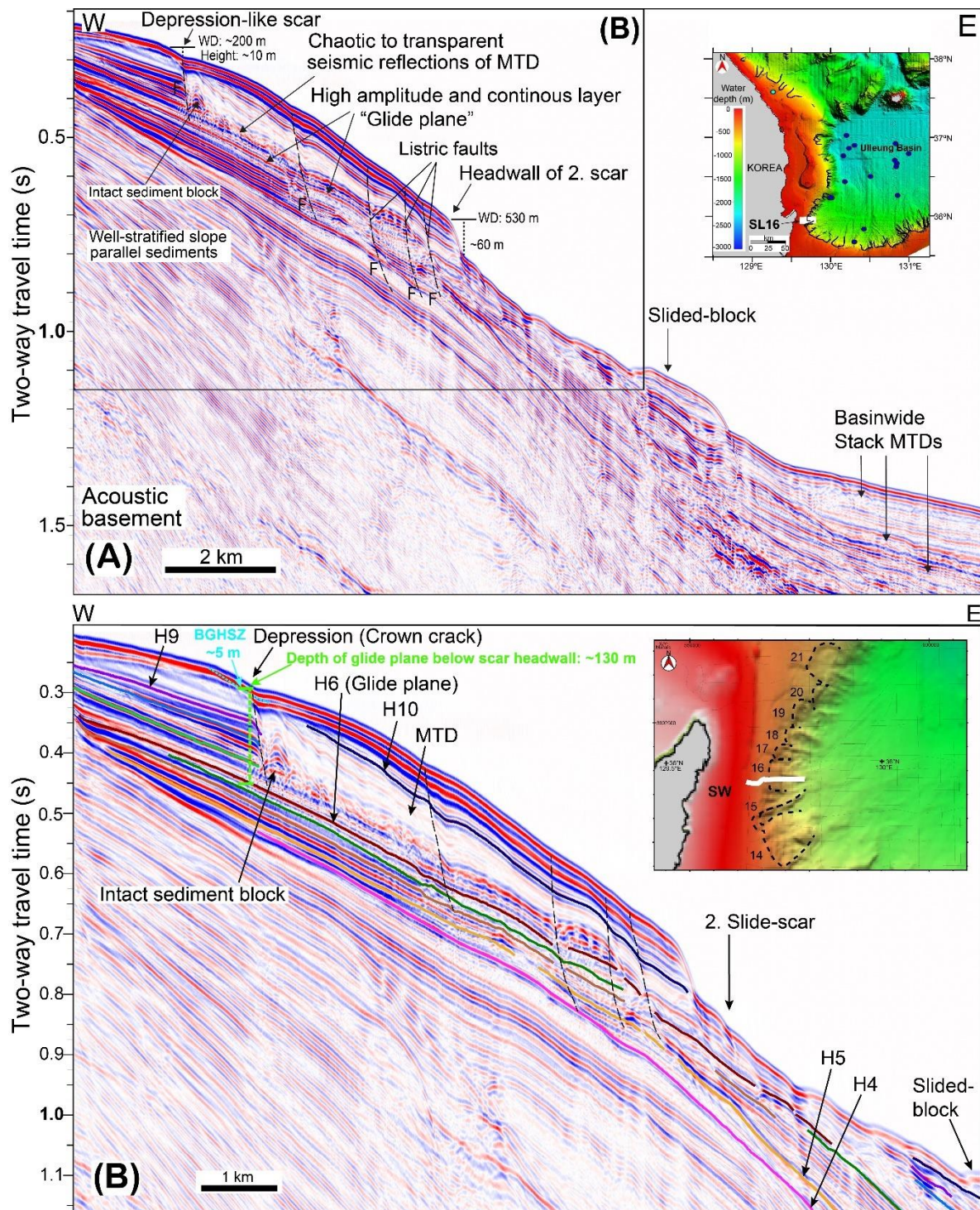
Figure 5. (A) W-E trending seismic profile traversing SL16 and displaying a buried slide scar in the upper slope (~185 mbsl) and a modern seafloor scar (~60 m high) in the lower slope (~520 mbsl water depth). The chaotic seismic reflections, interpreted as MTD units, are seen downslope of the headwall scarp. The seismic profile also shows an intact sediment block immediately below the headwall scar and numerous listric faults extending to the seafloor. Farther downslope, a prominent slide block, and numerous stacked MTDs are visible. **(B)** Close-up of the seismic profile shown in (A) displaying the tracked seismic horizons. H6, which sits beneath the MTD unit, forms the glide plane of SL16 and is characterized by a high-amplitude continuous seismic reflection parallel to the slope stratigraphy. The depth of the glide plane below the location of the uppermost scar (crown-crack/ depression) is about 130 m whereas the base of the gas hydrate stability zone in the area is ~5 m and pinching-out on the seafloor slightly upslope from this location (see Horozal et al., 2017, for details). The depths of glide planes and BGHSZ are listed for each profile in Table 2.
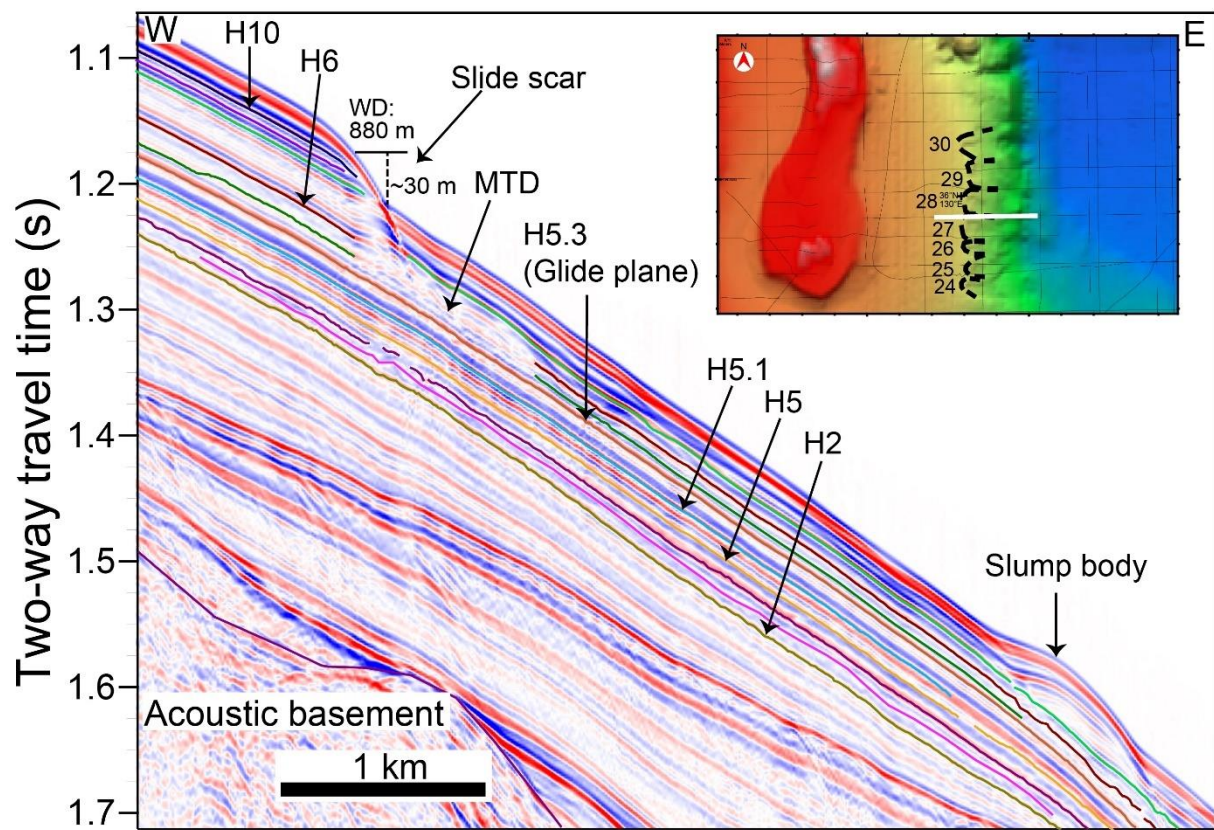
Figure 6. W-E –trending seismic profile traversing the SL27 on the western margin. H5.3, characterized by continuous high-amplitude reflection, represents the glide plane of SL27. The upper headwall of SL27 is about 30 m high. Adjacent to the eastern edge of the slide scar is a wedge-shaped MTD unit characterized by chaotic to transparent internal reflections. A prominent slump body with hummocky morphology is present further downslope.
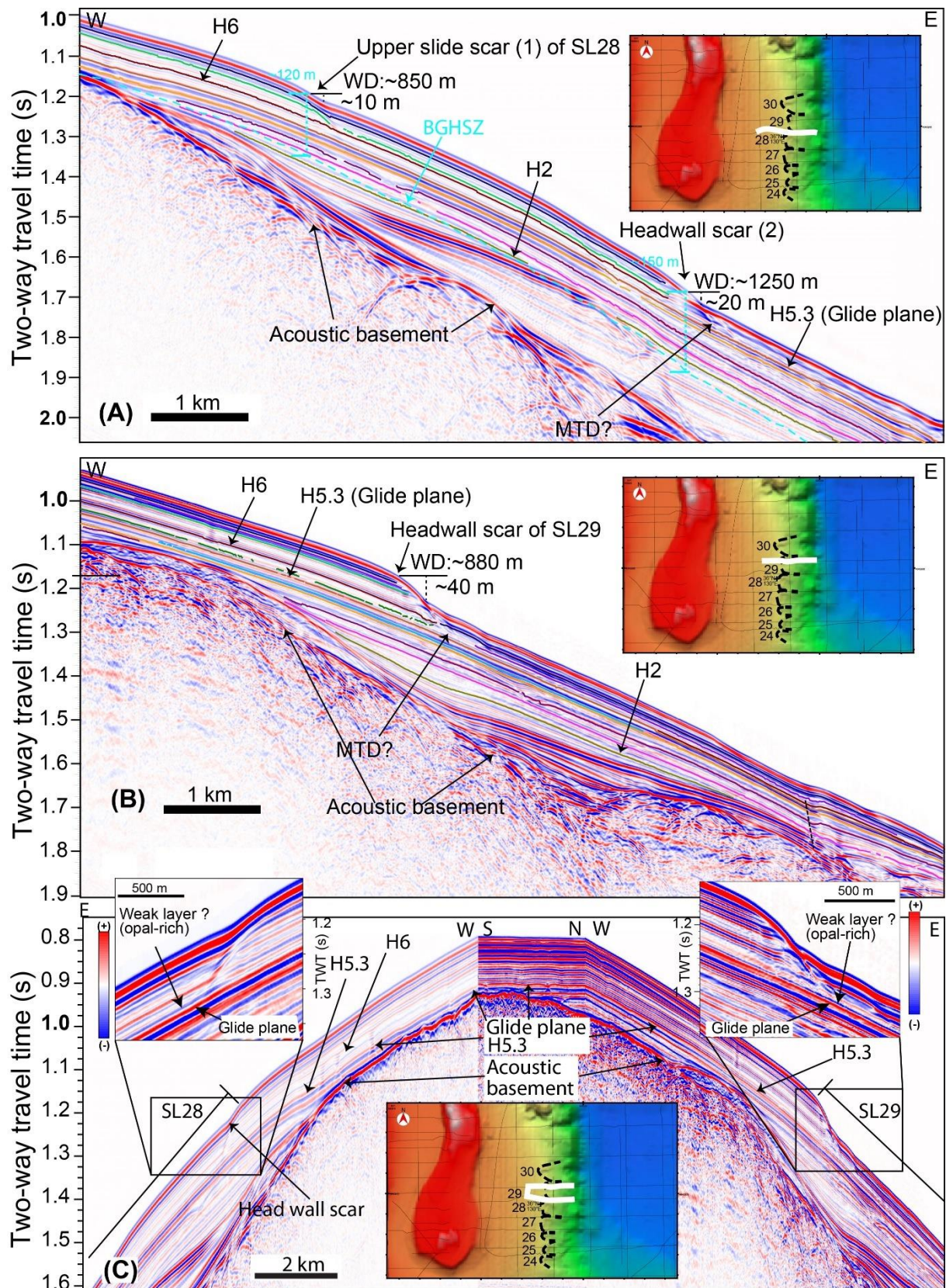
Figure 7. Seismic profiles across **(A)** SL28, **(B)** SL29, and **(C)** an arbitrary composite line tying the two profiles. Close up seismic profiles showing the high-amplitude positive polarity reflectors representing glide planes and the overlying negative polarity reflectors that probably corresponds to the opal-rich layers. See the inset maps for the line locations and figure 2 for the color codes to key seismic horizons. Note that both SL28 and SL29 share the same glide plane, H5.3.
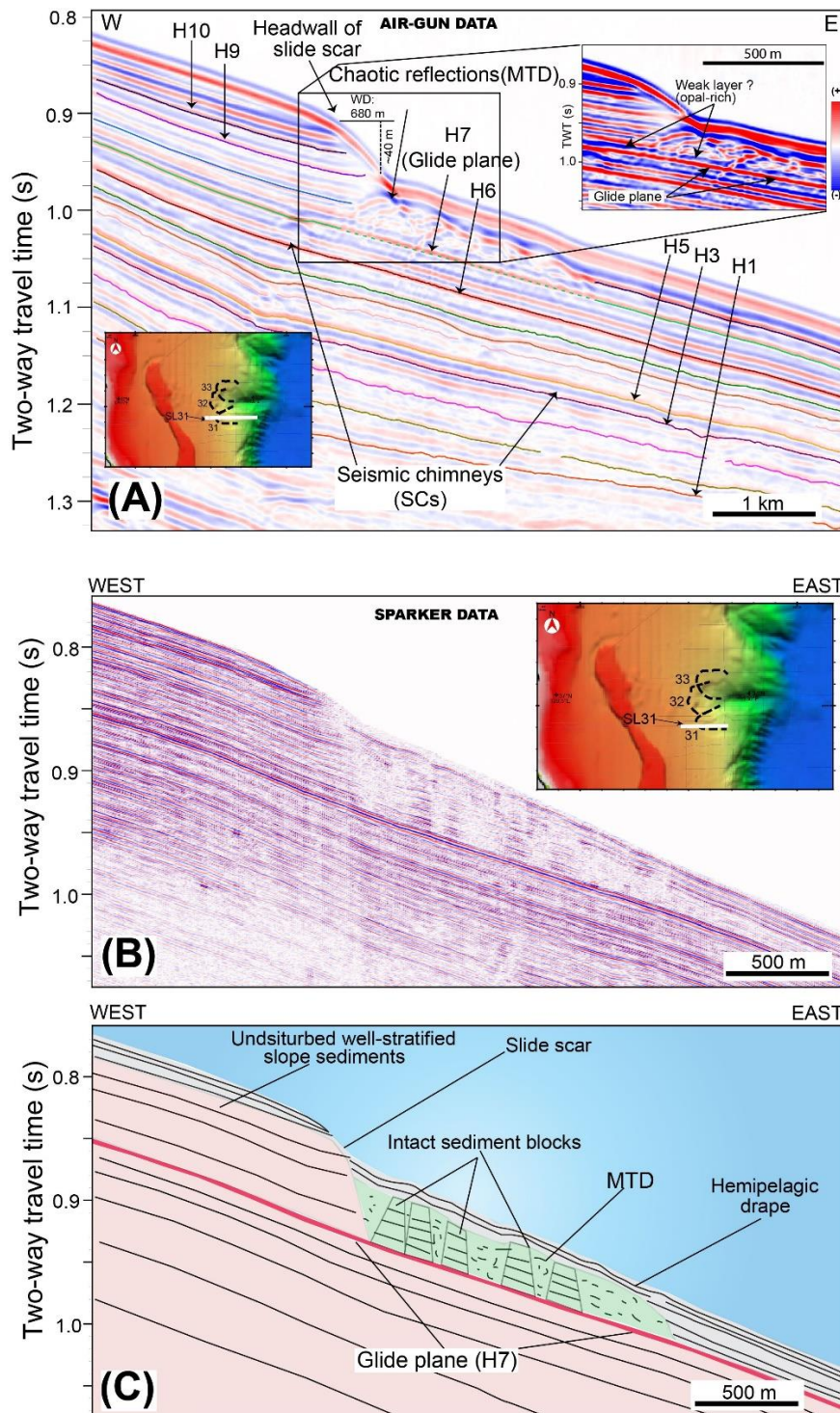
Figure 8. (A) W-E –trending air-gun seismic profile crossing SL31 and its headwall scar located at a seismic depth of 0.87 s (~650 m) with a height of 40 m. The base of the scar is characterized by chaotic seismic reflections extending about 2 km downslope that are typical characteristics of mass-transport deposits (MTDs). H7 (green horizon) forms the glide plane below the MTD. A close up seismic profile traversing the headwall scar area shows in detail the negative polarity reflector (possible weak layers) on top of the high-amplitude positive polarity reflector (glide planes). **(B)** High-resolution sparker profile crossing the crescent-shaped headwall scar of SL31 acquired nearby the air-gun profile shown in (A). The sparker profile images the internal reflection characteristics of the deformed sediments below the slide region and exhibits the presence of intact blocks with well-stratified internal reflections within the deformed material reflected by its chaotic/transparent character. **(C)** Interpretation of sparker profile illustrates undeformed sediment blocks and a distinct layer at the base of the MTD that acts as the glide plane. Note also the hummocky or irregular topography of the seafloor above the MTD unit.
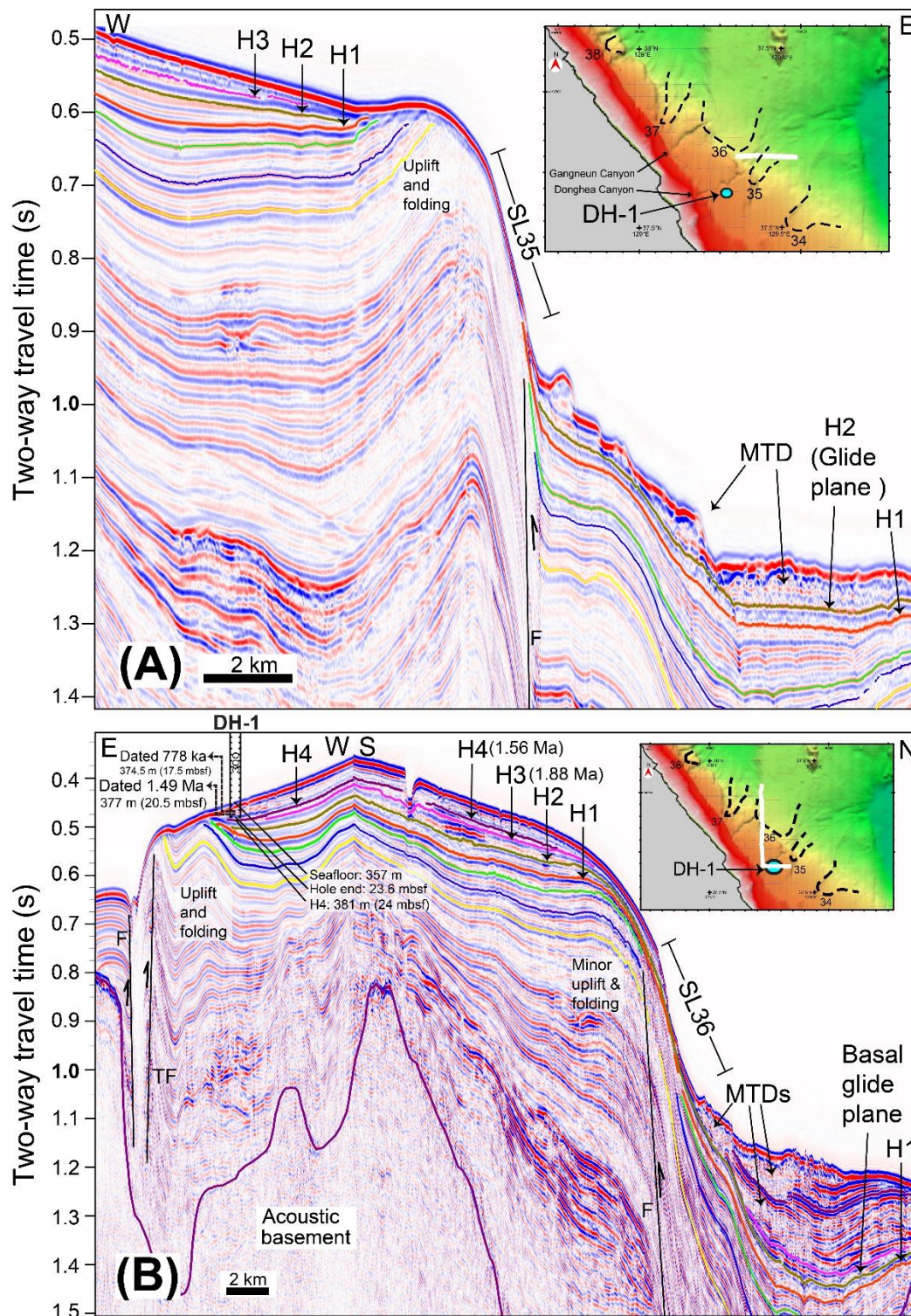
Figure 9. (A) Seismic profile from the northwestern margin traversing the SL35 in the W-E direction. H2 (olive horizon) corresponds to the glide plane of SL35 and separates chaotic seismic units above from well-stratified seismic units below. The headwall scarp of SL35 is located immediately below the folded and uplifted strata. **(B)** Arbitrary seismic profile crossing SL36 and hole DH-1. The headwall scar is found at the steepest eastern flank of the uplifted zone. Sequential multiple landslide events, as observed from multiple MTD units and glide planes, may have taken place at ca. 2.14 Ma, where H2 is defined as the basal glide plane which underlines the deepest MTD unit at the base of the slope. The Hole DH-1 was drilled and cored up to 23.6 m depth (Kwon et al., 2009) on the northwestern margin nearby SL35. Seismic- to core-tie is performed using acoustic velocities of sediment samples measured by Ryang et al. (2014).
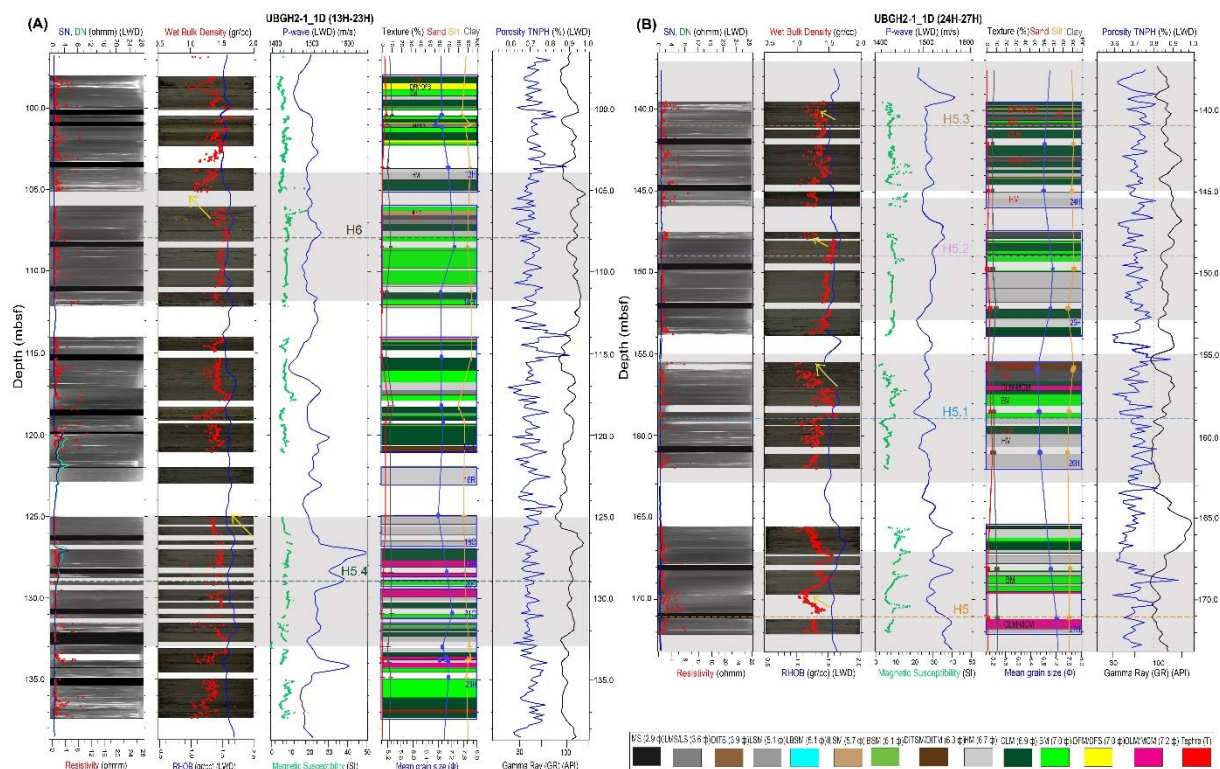
Figure 10. (A)-(B) X-radiographs and digital core images plotted with physical properties measured via LWD and on sediment samples of the drilling site UBGH2-1_1. The sedimentary units of cored sections consist of thin layers (<1 m thick) of BM interbedded with HM and CLM facies. Occasionally, facies of DFM/DFS and ILSM, LSM/LS, MS, and OLM/MCM occur as well. Silt is the dominant lithology (> 90%) throughout the cored interval. Generally, the inferred glide planes (dashed lines) are associated with higher bulk densities, GR, and P-wave velocities. In contrast, porosities show lower values at the glide planes. Yellow arrows mark the locations where densities show sharp decreases above the inferred glide planes. Glide planes are shaded in pink with an uncertainty of ±4 m owing to the vertical resolution of the seismic data.
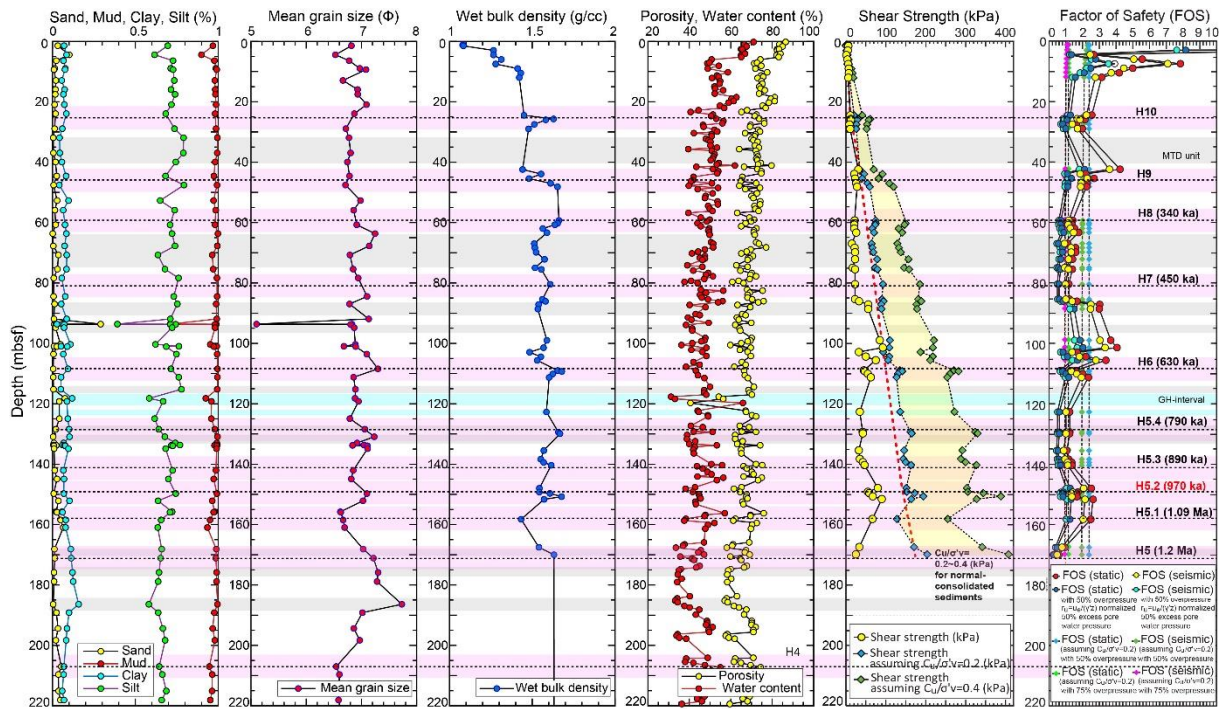
Figure 11. Vertical profiles of volume percent, mean grain size, wet bulk density, porosity, water content, undrained shear strength, and factor of safety (FOS) calculations under undrained conditions and for normally consolidated sediments (Cu/σ'v=0.2 and 0.4) from the core samples retrieved from the Hole UBGH2-1_1D. The sediments consist dominantly of silt. In a given sampling interval, variations in wet bulk density generally exist at the stratigraphic units above and below the inferred glide planes (e.g., H8, H7, H6, H5.4, H5.2, H5.1, and H5 marked with red dashed lines). Porosity and water contents decrease at units below and increase at units above the glide planes. Shear strength and FOS values drop drastically below about 108 mbsf, coinciding with the H6 glide plane. Our model calculations show that the present-day slope sediments <30 m are relatively stable under static (FOS$_{static}$ >1.0) and seismic conditions (FOS$_{seismic}$ >1.0). However, when including a 50% pore pressure, the FOS falls below 1.0 within the core depth of 25 m even under static conditions (FOS$_{static\ with\ overpressure}$). The red dashed line marks the lower limit of shear strength for normal consolidation (Cu/σ'v=0.2). Shaded zones in cyan represent potential gas hydrate-bearing layers while gray-shaded zones represent MTD units. Gray shaded lines represent upper and lower limit of glide planes with an interval of ±4 m owing to the vertical resolution of the seismic data.
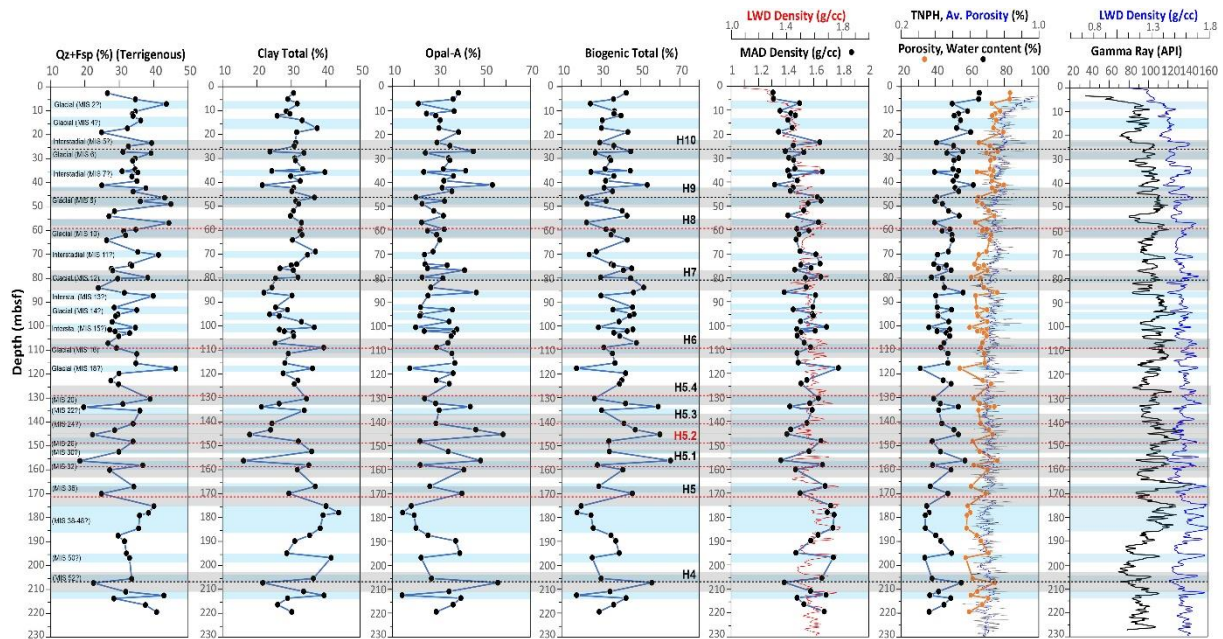
Figure 12. XRD mineralogical data and Moisture And Density (MAD) measurements of the Hole UBGH2-1_1D, and logging-while-drilling (LWD) gamma-ray (GR) and density and TNHP porosity measurements in the Hole UBGH2-1_1A. Overall, low Opal-A and biogenic total, representing the poorly-oxygenized dark muds formed during the glacial periods or sea-level low stands, are inversely correlated to the total Terrigenous and Clay contents. These intervals correspond to high density, low water content, and porosity. Blue bands on the plots represent inferred intervals of glacials or interstadials forming dark muds with higher clay and low biogenic Opal-A contents. Dashed lines denote inferred glide planes from H10 to H4, with MIS interpretations shown in figure 12. The blue curve over the TNHP log in black represents the moving average of TNHP porosity. Gray shaded lines are the upper and lower limit of the glide planes with an interval of ±4 m owing to the vertical resolution of the seismic data.
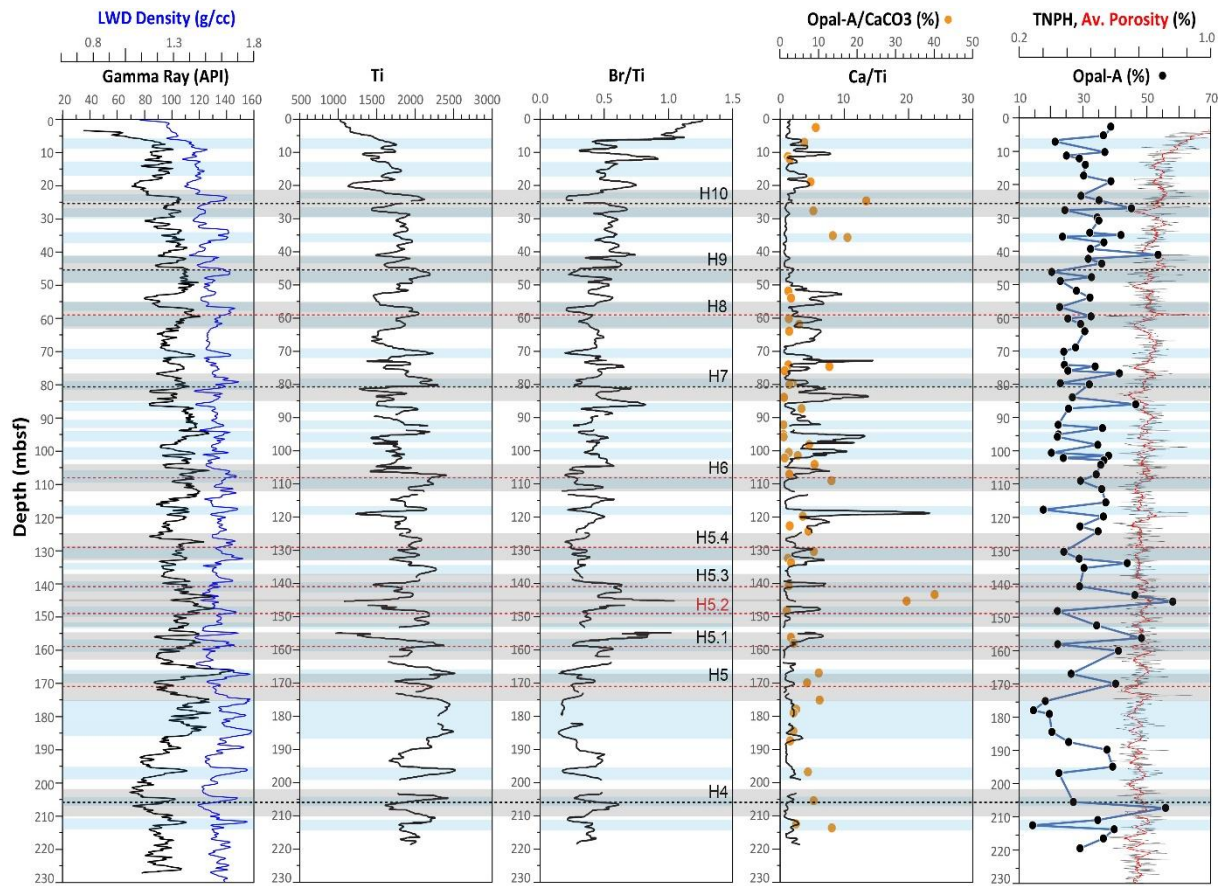
Figure 13. Comparison of LWD density, GR and TNPH porosity logs, Opal-A, and XRF readings of elements and their fractions (Ti, Br/Ti, Ca/Ti) in relation to the inferred glide planes (dashed lines). Ti represents detrital particles. Br/Ti is an indication of biogenic (algal) productivity and Ca/Ti is a proxy for biogenic calcium carbonate content. The inferred glide planes correlate with intervals of high density and GR logs, high Ti fraction, low Opal-A and porosities, and low fractions of Br/Ti and Ca/Ti. Gray shaded lines correspond to the upper and lower limit of the glide planes with an interval of ±4 m owing to the vertical resolution of the seismic data.
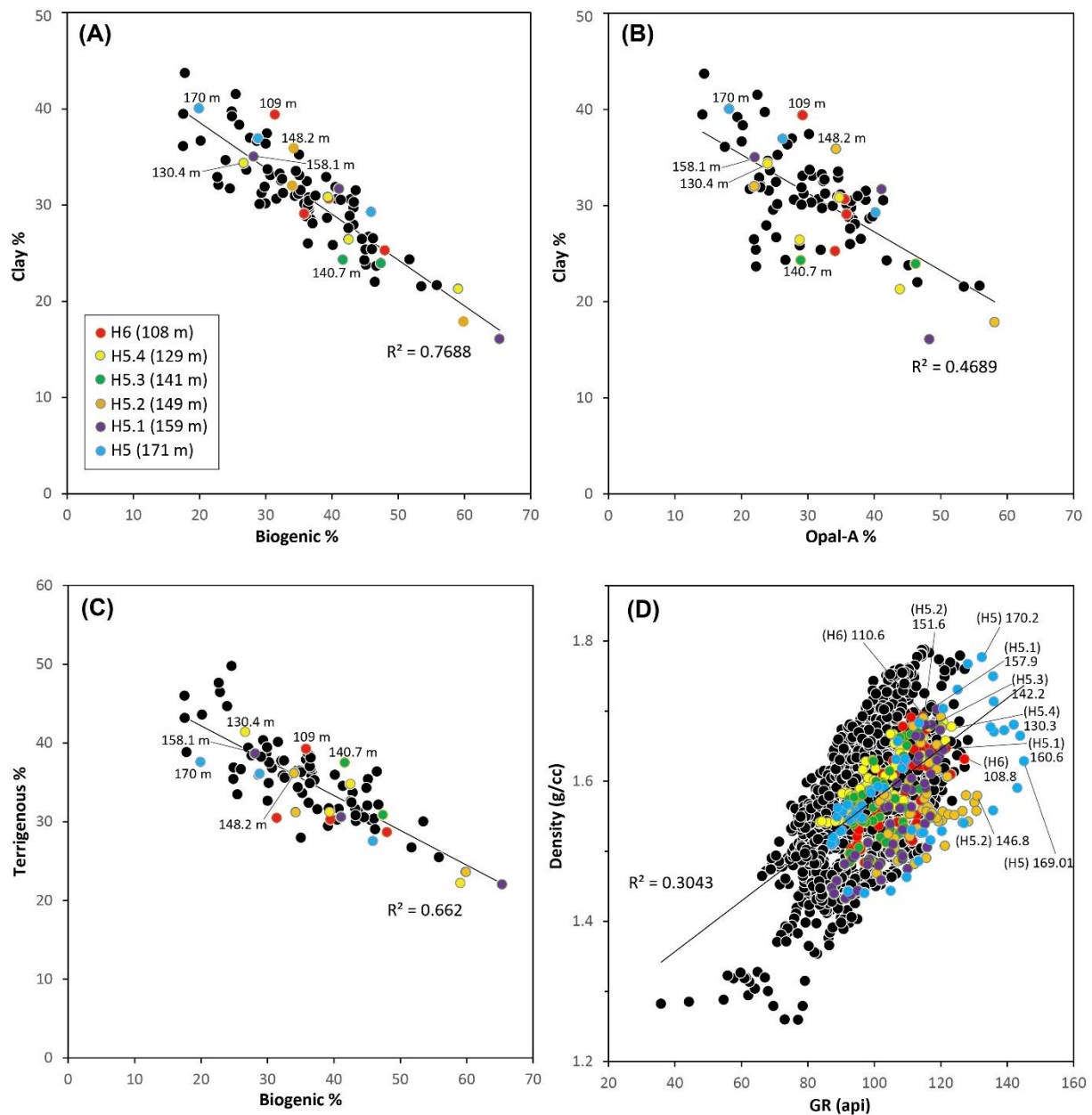
Figure 14. XRD cross-plots of total clay vs. total biogenic **(A)**, opal-A vs. clay **(B)**, total terrigenous vs. total biogenic contents **(C)**, and LWD density vs. GR **(D)**. The black points are background data (0–171 mbsf) and the colored data points represent the values within ±4 m depth interval of the tracked horizons between H6 and H5 (108–171 mbsf, depths shown in legend). Labeled depths of data points represent the highest clay (A-B), terrigenous (C), and density and GR contents (D) as errors between them and horizon depths are generally in less than ±1 m range due to sampling intervals. The sedimentary beds associated with glide planes are mainly concentrated in the end members of the compositional continuum of the sediments (i.e., high clay, density, and GR).
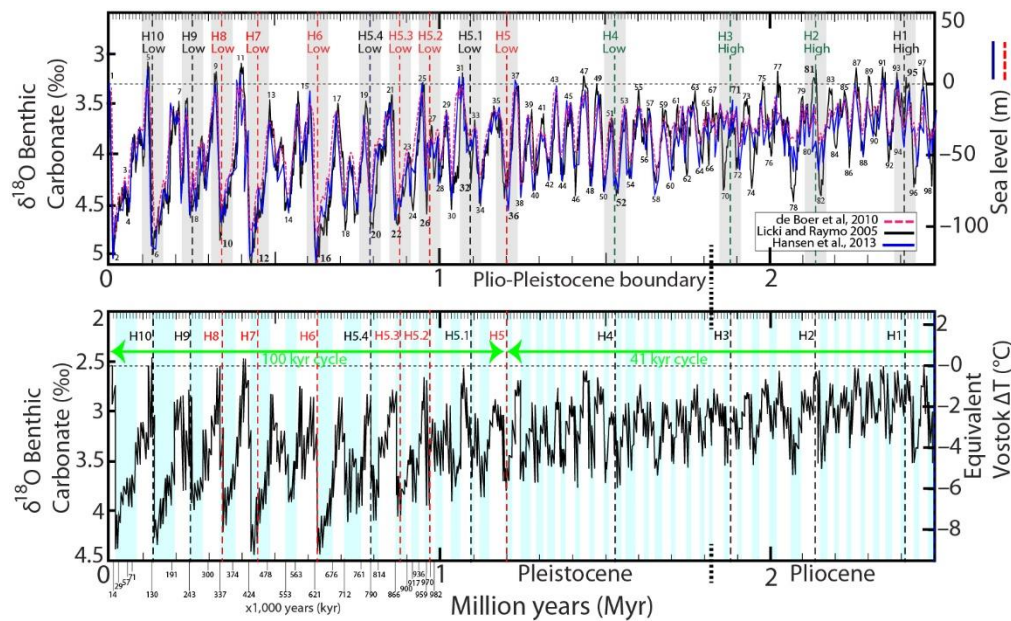
Figure 15. Modeled sea-level change curves studied by Lisiecki and Raymo (2005), de Boer et al. (2010), and Hansen et al. (2013) since the Late Pliocene (2.5 Ma), and global temperature changes in equivalent Vostok temperature gradients (degrees Celcius) inferred based on changes in δ¹⁸O benthic carbonate in ocean sediments with marine isotope stages (shown with numbers) from Lisiecki and Raymo (2005) (at the bottom). Dashed lines denote interpreted horizons from 1 to 10 (H1 – H10) from older to younger, respectively. Dashed lines in red locate the ages of some of the common glide planes (defined as H8, H7, H6, H5.4 H5.3, H5.2, and H5) in the western, southern, and southwestern margins. The glide planes of submarine landslides in the northwestern margin (i.e., H4, H3, and H2 marked by green dashed lines) are estimated to be older than H5, ranging in age between 1.5 – 2.14 Ma. Gray bands on the top plot represent the error range of age (±35 ky). Cyan-colored bands plot at the bottom represent glacial intervals in the last Plio-Quaternary.

Tables

Main Horizons	Sub-horizons	Age (ca.)	Depth (mbsf)	Interval
H10 (navy)		130 ka	26 m	
H9 (purple)		250 ka	47 m	+120 k
H8 (blue)		**340 ka**	**59 m**	+90 k
H7 (green)		**450 ka**	**81 m**	+110 k
H6 (brown)		**630 ka**	**108 m**	+180 k
	H5.4 (emerald)	**790 ka**	**129 m**	+160 k
	H5.3 (tan)	**880 ka**	**141 m**	+100 k
	H5.2 (light pink)	**970 ka**	**149 m**	+110 k
	H5.1 (sky)	1,090 ka	159 m	+90 k
H5 (orange)		**1,200 ka**	**171 m**	+110 k
H4 (violet)		1,530 ka	207 m	+330 k
H3 (pink)		1,880 ka	245 m	+350 k
H2 (olive)		2,140 ka	280 m	+260 k
H1 (red)		2,410 ka	308 m	+270 k

Table 1. List of the correlative seismic horizons, their estimated ages based on the seismic-to-well tie, and depths in meters below seafloor (mbsf) at the drilling site UBGH2-1_1. Seismic horizons marked in the bold text correspond to the major glide planes of the submarine landslides defined in the western and southwestern margins (SL16-33). The glide planes of submarine landslides in the northwestern margin (SL34-37) are correlated to be older (H5 and older; ≥1200 ka) than those of the western and southwestern counterparts.

| Sub-marine land-slide number	(a) Glide planes		(b) Depth of base of GHSZ below scar headwall (mbsf)	(c) Submarine landslide scars	
	(1) Horizon number	(2) Depth below scar headwall (mbsf)		(1) Water depth of scar headwall (mbsl)	(2) Height of scar headwall (mbsl)
Southwestern margin					
SL14	H6	120	60	190	250
SL15	H6	100	20	260	150
SL16	H6	130	5	210 (depression) 530 (MBES: 510)	10 60 (MBES: 80)
SL17	H6	130	45	385	70
SL18	H6	80	50	535	100
SL19	H5	75	30	260 (depression) 600 (MBES)	40 75 (MBES)
SL20	H6	65	115	420 820 (MBES)	20 60
SL21	H5.2	120	100	480 (MBES:600)	50
SL22	H5.2	130	85	670 (MBES:1030)	110
SL23	H5.2	65	106	870	50
Western margin					
SL24	H5.4	75	145	830	75
SL25	H5.3 & H5	90	165	880	70
SL26	-	-	-	855	45
SL27	H5.3	110	120	880 (MBES: 830)	30 (MBES: 70)
SL28	H6 H5.3	40 50	120 150	850 (MBES: 848) 1200	10 (MBES: 40) 20
SL29	H5.3	40	90	880 (MBES: 830)	40 (MBES: 55)
SL30	-			782 (MBES)	65
SL31	H7	85	85	680 (MBES: 622)	40 (MBES: 30)
SL32	H8	85	100	550	60
SL33	H8	65	105	695	70
Northwestern margin					
SL34	H5	95	140	450	90
SL35	H2	65	80	492	65
SL36	H4 H3 H2	50 (multiple glide planes)	80	540	190
SL37	H3	95	75	365	60
SL38	-	-	-	150	60

Table 2. List of corresponding seismic horizon and depth below headwall scar of the glide plane of each submarine landslide in the margins of Ulleung Basin. For locations of the numbered submarine landslides, see figure 1C. Also indicated are the depths of the base of gas hydrate stability zone (BGHSZ) below the headwall scars, and the water depths and heights of the headwall scarps.

Supplementary figures
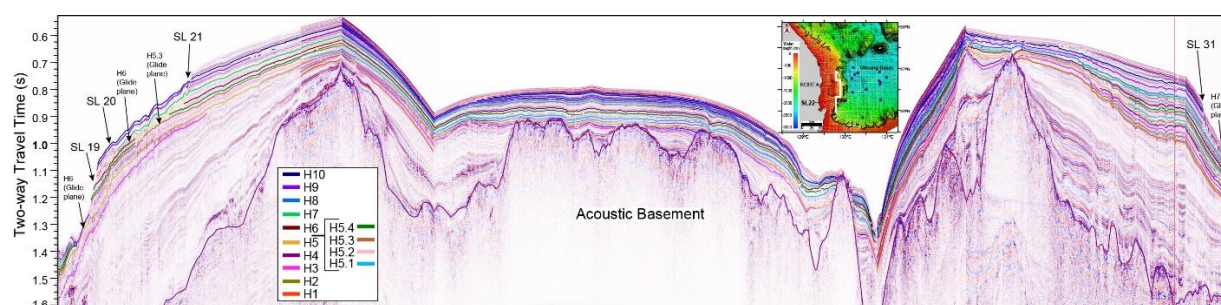
Figure S1. An arbitrary seismic profile traversing through the western margin. This arbitrary line and the parallel crossing lines were used to track the key seismic horizons throughout the southwestern, western, and northwestern margins.
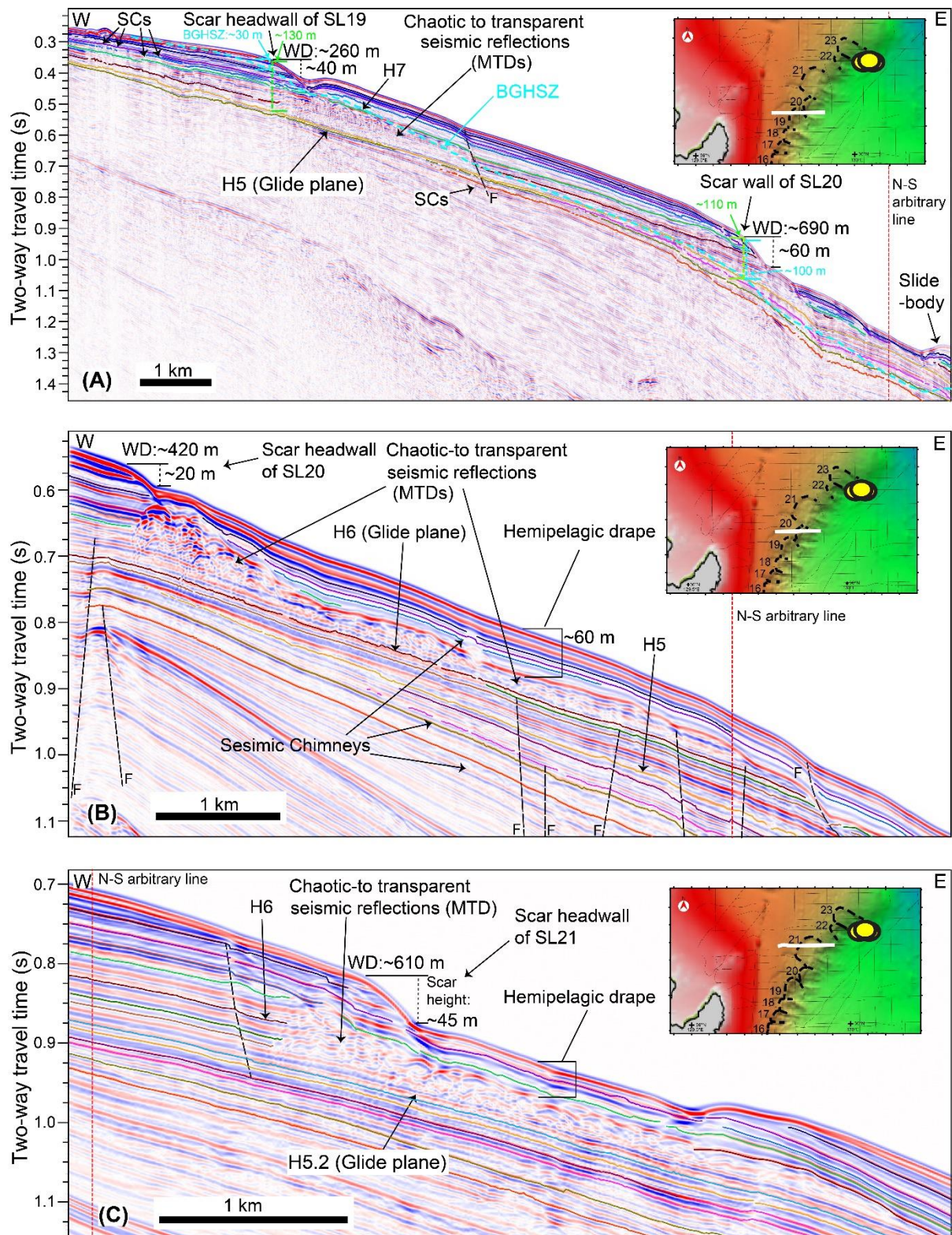
Figure S2. (A-C) W-E –trending seismic profiles crossing SL19, SL20, and SL21 on the southwestern margin. H5, H6, and H5.2 sit beneath the SL19, SL20, and SL21, respectively. The overlying MTD units show eastward thinning wedge-shaped geometries with chaotic to transparent internal seismic facies. Well-stratified seismic reflections blanket the MTDs. The headwall scarps of SLs form a step-like morphology on the modern seafloor with a maximum height of 45 m.
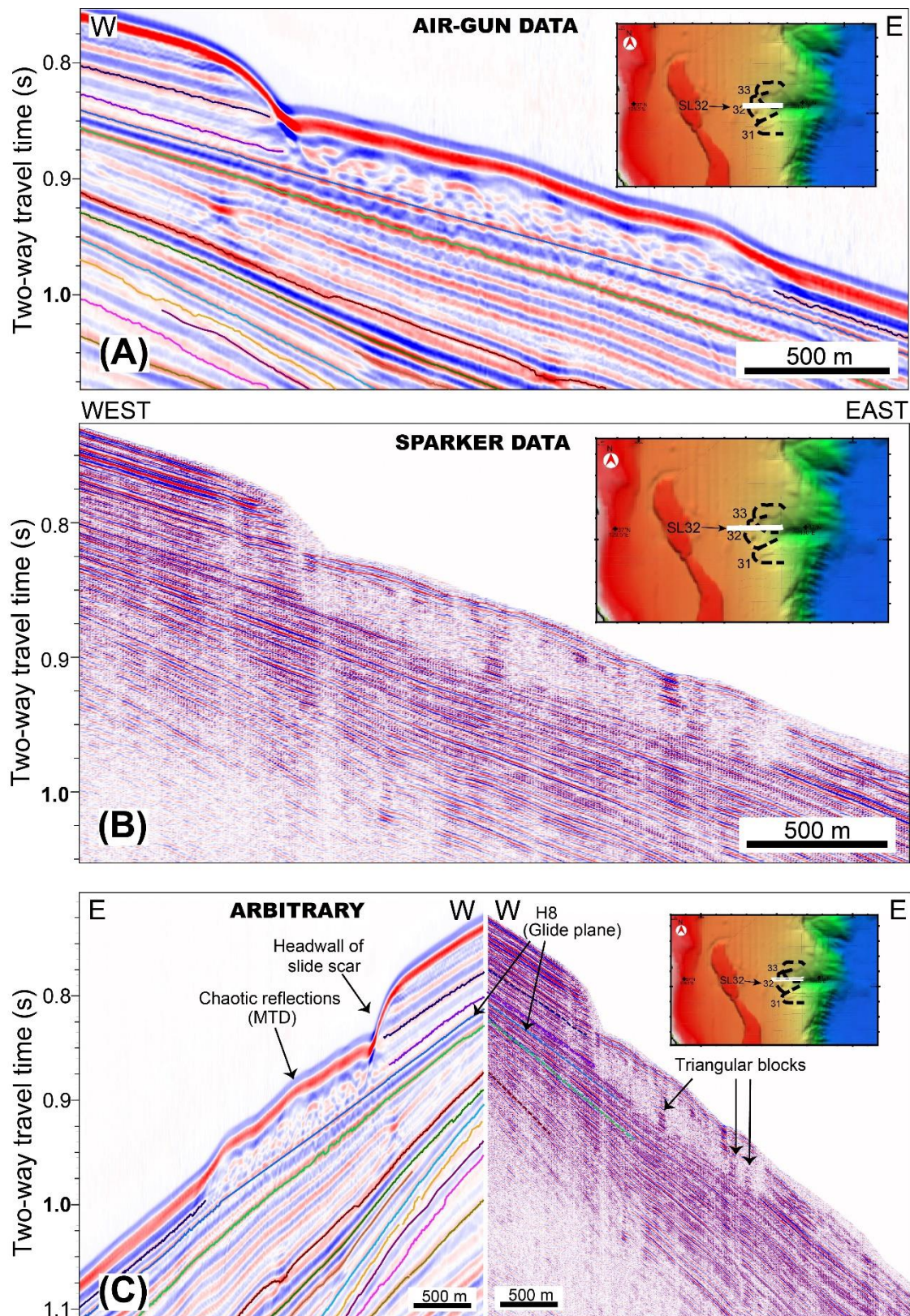
Figure S3. W-E –trending air-gun seismic profile (A), sparker profile (B), and their tie line (C) crossing SL32, its headwall scar, and associated MTD units characterized by chaotic reflections. H8 forms the glide plane of the SL32. Noteworthy also is the presence of triangular sediment blocks within the MTD unit.

Supplementary tables (available online)

Table S1. The age-depth correlations defined by seismic to well ties from the study of Bahk et al. (2016) and this study. Bold texts are ages (ka) and depths (mbsf) correlated with refined synthetic seismograms in this study showing that they are overall in good agreement with depths- ages correlated by Bahk et al. (2016).

Table S2. Sedimentary Facies.

Table S3. Sedimentary facies above and below glide planes.

References

Alves, T.M., 2015. Submarine slide blocks and associated soft-sediment deformation in deep-water basins: A review. Marine and Petroleum Geology 67, 262–285. https://doi.org/10.1016/j.marpetgeo.2015.05.010

Badhani, S., Cattaneo, A., Collico, S., Urgeles, R., Dennielou, B., Leroux, E., Colin, F., Garziglia, S., Rabineau, M., Droz, L., 2020. Integrated geophysical, sedimentological and geotechnical investigation of submarine landslides in the Gulf of Lions (Western Mediterranean). Geological Society, London, Special Publications 500, 359–376. https://doi.org/10.1144/SP500-2019-175

Baeten, N.J., Laberg, J.S., Forwick, M., Vorren, T.O., Vanneste, M., Forsberg, C.F., Kvalstad, T., Ivanov, M., 2013. Morphology and origin of smaller-scale mass movements on the continental slope off northern Norway, Geomorphology 187, 122–134. https://doi.org/10.1016/j.geomorph.2013.01.008

Baeten, N.J., Laberg, J.S., Vanneste, M., Forsberg, C.F., Kvalstad, T.J., Forwick, M., Vorren, T.O., Haflidason, H., 2014. Origin of shallow submarine mass movements and their glide planes— Sedimentological and geotechnical analyses from the continental slope off northern Norway. J. Geophys. Res. Earth Surf. 119, 2335–2360. https://doi.org/10.1002/2013JF003068

Bahk, J.-J., Chough, S.-K., Han, S.-J., 2000. Origins and paleoceanographic significance of laminated muds from the Ulleung Basin, East Sea (Sea of Japan). Marine Geology 162, 459– 477. https://doi.org/10.1016/S0025-3227(99)00079-1

Bahk, J.J., Kim, G.Y., Chun, J.H., Kim, J.H., Lee, J.Y., Ryu, B.J., Lee, J.H., Son, B.K., Collett, T.S., 2013. Characterization of gas hydrate reservoirs by integration of core and log data in the Ulleung Basin, East Sea. Marine and Petroleum Geology 47, 1–13. https://doi.org/10.1016/j.marpetgeo.2013.05.007

Bahk, J.-J., Um, I.-K., Yi, B.-Y., Yoo, D.-G., 2016. Paleoceanographic implications and cyclostratigraphy of variations in well-log data from the western slope of the Ulleung Basin, East Sea. Quaternary International 392, 58–68. https://doi.org/10.1016/j.quaint.2015.08.023

Bahk, J.-J., Um, I.-K., Jang, J.-H., 2021. Lateral sediment transport and late Quaternary changes of eolian sedimentation in the East Sea (Japan Sea). Journal of Asian Earth Sciences 208, 104672. https://doi.org/10.1016/j.jseaes.2021.104672

Bryant, W.R., Bennett, R.H., Katherman, C.E., 1981. Shear strength, consolidation, porosity, and permeability of oceanic sediments, In: Emiliani, C. (ed.), The Sea, Volume 7: The Oceanic Lithosphere, New York, John Wiley & Sons, p. 1555–1616.

Bryn, P., Solheim, A., Berg, K., Lien, R., Forsberg, C.F., Haflidason, H., Ottesen, D., Rise, L., 2003. The Storegga Slide complex; repeated large scale sliding in response to climatic cyclicity. In: Locat, J., Mienert, J. (Eds.), Submarine Mass Movements and their Consequences. Kluwer Academic Press, The Netherlands, pp. 215–222.

Bull, S., Cartwright, J., Huuse, M., 2009. A subsurface evacuation model for submarine slope failure. Basin Research 21(4), 433–443. https://doi.org/10.1111/j.1365-2117.2008.00390.x

Casalbore, D., Bosman, A., Ridente, D., Chiocci, F., Ingrassia, M., Macelloni, L., Sposato, A., Martorelli, E., 2016. Coastal and submarine landslides in the tectonically-active Tyrrhenian Calabrian margin (Southern Italy): Examples and geohazard implications. In Submarine Mass Movements and Their Consequences. Advances in Natural and Technological Hazards Research; Krastel, S., Ed.; Springer: Heidelberg, Germany; Cham, Switzerland, Volume 37, pp. 261–269. https://doi.org/10.1007/978-3-319-00972-8_23

Chopra, S., Castagna, J., Portniaguine O., 2006. Seismic resolution and thin-bed reflectivity inversion. CSEG Recorder 1, 19-25.

Chough, S.K., and Lee, H.J., 1987. Stability of sediments on the Ulleung basin slope. Marine Geotechnology 17, 123–132.

Chough, S.K., Lee, H.J., Yoon, S.H., 2000. Marine Geology of Korean Seas, second edition. Elsevier, Amsterdam. pp. 313. https://doi.org/10.1016/B978-0-444-50438-8.X5010-3

Cukur, D., Kim, S.-P., Kong, G.-S., Kim, J.-K., Bahk, J.-J., Horozal, S., Um, I.-K., Lee, G.-S., Chang, T.-S., Ha, H.-J., Völker, D., Kim, J.-K., 2016. Geophysical evidence and inferred triggering factors of submarine landslides on the western continental margin of the Ulleung Basin. East Sea. Geo. Mar. Lett. 36 (6), 425–444. https://doi.org/10.1007/s00367-016-0463-5

Cukur, D., Um, I.-K., Chun, J.-H., Kim, S.-R., Lee, G.-S., Kim, Y., Kong, G.-S., Horozal, S., Kim, S.-P., 2018. A multi-factor approach for process-based seabed characterization: example from the northeastern continental margin of the Korean peninsula (East Sea). Geo-Mar. Lett. 38, 323–339. https://doi.org/10.1007/s00367-018-0537-7

Cukur, D., Um, I.-K., Chuna, J.-H., Lee, G.-S., Kim., S.-R., Bahk, J.-J., Urgeles, R., Horozal, S., 2020. Factors leading to slope failure on a sediment-starved margin: The southwestern continental margin of the East Sea, Korea. Marine Geology 428, 106282, 1–21. https://doi.org/10.1016/j.margeo.2020.106282

Dan, G.; Sultan, N.; Savoye, B., 2007. The 1979 nice harbour catastrophe revisited: Trigger mechanism inferred 969 from geotechnical measurements and numerical modelling. Marine Geology 245,

40–64. https://doi.org/10.1016/j.margeo.2007.06.011

De Blasio, F.V., Elverhøi A., Issler, D., Harbitz, C.B., Bryn, P., Lien, R., 2004: Flow Models of natural debris flows originating from over consolidated clay materials. Marine Geology 213, 439–455.

De Blasio, F.V., Elverhøi, A., Engvik, L.E., Issler, D., Gauer, P., Harbitz, C., 2006. Understanding the high mobility of subaqueous debris flows. Norwegian Journal of Geology 86, 275–284.

De Boer, B., Van de Wal, R.S.W., Bintanja, R., Lourens, L.J., Tuenter, E., 2010. Cenozoic global ice volume and temperature simulations over the past 40 million year. Pangaea. https://doi.org/10.1594/PANGAEA.859149.

Elverhøi, A., Harbitz, C., Dimakis, P., Mohrig, D., Marr, J., Parker, G., 2000. On the dynamics of subaqueous debris flows. Oceanography 13, 109.

Gatter R., Clare M.A., Hunt J.E., Watts M., Madhusudhan B.N., Talling P.J., Huhn K., 2020. A multi-disciplinary investigation of the AFEN Slide: the relationship between contourites and submarine landslides. Geological Society, London, Special Publications 500, pp. http://doi.org/10.1144/SP500-2019-184

Goldberg, D., 1997. The role of the downhole measurements in marine geology and geophysics. Reviews of Geophysics 35, 315–342. https://doi.org/10.1029/97RG00221

Gross, F., Mountjoy, J.J., Crutchley, G.J., Böttner, C., Koch, S., Bialas, J., Pecher, I., Woelz, S., Dannowski, A., Micallef, A., Huhn, K., Krastel, S., 2018. Free gas distribution and basal shear zone development in a subaqueous landslide—insight from 3D seismic imaging of the Tuaheni Landslide Complex, New Zealand. Earth and Planetary Science Letters 502, 231–243. https://doi.org/10.1016/j.epsl.2018.09.002

Hampton, M.A., Lee, H.J., Locat, J., 1996. Submarine landslides. Reviews of Geophysics 34, 33–59. https://doi.org/10.1029/95RG03287

Hansen, J., Sato, M., Russell, G., Kharecha, P., 2013. Climate sensitivity, sea level, and atmospheric carbon dioxide. Phil. Trans. Roy. Soc. A. 371, 20120294. https://doi.org/10.1098/rsta.2012.0294.

Harders, R., Kutterolf, S., Hensen, C., Moerz, T., Brueckmann, W., 2010. Tephra layers: a controlling factor on submarine translational sliding? Geochem. Geophys. Geosyst. 11 (7), Q07S25. http://dx.doi.org/10.1029/2009GC002844

Horozal, S., Kim, G.Y., Bahk, J.J., Wilkens, R.H., Yoo, D.G., Ryu, B.J., Kim, S.P., 2015. Core and sediment physical property correlation of the second Ulleung Basin Gas Hydrate Drilling Expedition (UBGH2) results in the East Sea (Japan Sea). Marine and Petroleum Geology 59,

535–562. http://dx.doi.org/10.1016/j.marpetgeo.2014.09.019

Horozal, S., Bahk, J.J., Lee, S.H., Urgeles, R., Kim, S.P., Kim, G.Y., Cukur, D., Lee, G.H., Ryu, B.J., Kim, J.H., 2016. Late Neogene-Quaternary submarine mass wasting along the margins of the Ulleung Basin, East Sea: geomorphologic controls and geohazard potential. Quaternary International 392, 69–98. http://dx.doi.org/10.1016/j.quaint.2015.06.056

Horozal, S., Bahk, J.J., Urgeles, R., Kim, G.Y., Cukur, D., Kim, S.P., Lee, G.H., Lee, S.H., Ryu, B.J., Kim, J.H., 2017. Mapping gas hydrate and fluid flow indicators and modeling gas hydrate stability zone (GHSZ) in the Ulleung Basin, East (Japan) Sea: potential linkage between the occurrence of mass failures and gas hydrate dissociation. Marine and Petroleum Geology 80, 171–191. http://dx.doi.org/10.1016/j.marpetgeo.2016.12.001

Horozal, S., Bahk, J.-J., Lee, S.H., Cukur, D., Urgeles, R., Kim, G.Y., Kim, S.-P., Ryu, B.-J., Kim, J.-H., 2018. Mass-wasting processes along the margins of the Ulleung Basin, East Sea: insights from multichannel seismic reflection and multibeam echosounder data. In: Subaqueous Mass Movements and their Consequences: Advances in Process Understanding, Monitoring and Hazard Assessments, D.G Lintern, D.C. Mosher, L.C. Moscardelli et al. [Eds]. Geological Society, London, Special Publications 477, 107–120. https://doi.org/10.1144/SP477.18

Irino, T., and Tada, R. 2002. High-resolution reconstruction of variation in Aeolian dust (Kosa) deposition at ODP site 797, the Japan Sea, during the last 200 ka. Global and Planetary Change 35, 143–156.

Irino, T., and Tada, R., 2003. High-resolution reconstruction of variation in aeolian dust (Kosa) deposition at ODP site 797, the Japan Sea, during the last 200 ka. Global and Planetary Change 35, 143–156. https://doi.org/10.1016/S0921-8181(02)00135-2

Issler, D., De Blasio, F.V., Elverhøi, A., Bryn, P., & Lien, R., 2005. Scaling Behavior of clay-rich submarine debris flows. Marine and Petroleum Geology 22, 187–194.

Jeong, S.W., 2010. Grain size dependent rheology on the mobility of debris flows. Geoscience Journal 14, 359.

Jeong, S.-W., Urgeles, R., Bahk, J.-J., Yoo, D.-G., Lee, G.-S., 2022. Rheological characteristics of marine sediments from the Ulleung Basin, East Sea to estimate the mobility of submarine landslides. Marine Geophysical Research 43, 16. doi:10.1007/s11001-022-09473-1

Khim, B.K., Bahk, J.J., Hyun, S., Lee, G.H., 2007. Late Pleistocene dark laminated mud layers from the Korea Plateau, western East Sea/Japan Sea, and their paleoceanographic implications. Palaeogeography, Palaeoclimatology, Palaeoecology 247, 74–87.

https://doi.org/10.1016/j.palaeo.2006.11.029

Kido, Y., Minami, I., Tada, R., Fujine, K., Irino, T., Ikehara, K., Chun, J.H., 2007. Orbital-scale stratigraphy and high-resolution analysis of biogenic components and deepwater oxygenation conditions in the Japan Sea during the last 640 kyrs using XRF microscanner. Palaeogeography, Palaeoclimatology and Palaeoecology 247, 32–49. https://doi.org/10.1016/j.palaeo.2006.11.020

KIGAM (Korea Institute of Geoscience and Mineral Resources), 2007. Report Studies on Geophysical Exploration of Gas Hydrate. Report of Korea Institute of Geosciences and Mineral Resources, NP2007-020-2007(1). Korea, 649 pp.

KIGAM (Korea Institute of Geoscience and Mineral Resources), 2011. Studies on Gas Hydrate Geology and Geochemistry Report. KIGAM, Daejeon, Korea, x pp.

Krastel, S., Li, W., Urlaub, M., Georgiopoulou, A., Wynn, R.B., Schwenk, T., Stevenson C., Feldens, P., 2018. Mass wasting along the NW African continental margin. Geological Society, London, Special Publications 477, 151–167. https://doi.org/10.1144/SP477.36

Kvalstad, T.J., Andresen, L., Forsberg, C.F., Berg, K., Bryn, P., Wangen, M., 2005. The Storegga slide: evaluation of triggering sources and slide mechanics. Marine and Petroleum Geology 22, 245–256. https://doi.org/10.1016/j.marpetgeo.2004.10.019

Kwon, Y.K., Yoon, S.H., and Chough, S.K., 2009. Seismic stratigraphy of the western South Korea Plateau, East Sea: implications for tectonic history and sequence development during back-arc evolution. Geo-Marine Letters 29, 181–189. https://doi.org/10.1007/s00367-009-0133-y

L'Heureux, J.-S., Longva, O., et al. 2012. Identification of Weak Layers and Their Role for the Stability of Slopes at Finneidfjord, Northern Norway. In: Submarine Mass Movements and Their Consequences. Dordrecht, Springer Netherlands, 321–330., https://doi.org/10.1007/978-94-007-2162-3_29.

Laberg, J.S., Dahlgren, T., Vorren, T.O., Haflidason, H., Bryn, P., 2001. Seismic analyses of Cenozoic contourite drift development in the Northern Norwegian Sea. Marine Geophysical Researches 22, 401–416.

Laberg, J.S., and A., Camerlenghi, 2008. The Significance of Contourites for Submarine Slope Stability. Developments in Sedimentology 60, 537–556. https://doi.org/10.1016/S0070-4571(08)10025-5

Lee, G.H., and B.C., Suk, 1998. Latest Neogene-Quaternary seismic stratigraphy of the Ulleung Basin, East Sea (Sea of Japan). Marine Geology 146, 205–224. https://doi.org/10.1016/S0025-3227(97)00123-0

Lee, G.H., Kim, H.J., Han, S.J., Kim, D.C., 2001. Seismic stratigraphy of the deep Ulleung Basin in the East Sea (Japan Sea) back-arc basin. Mar. Pet. Geol. 18, 615–634. https://doi.org/10.1016/S0264-8172(01)00016-2

Lee, S.H., Bahk, J.J., Kim, H.H., Kim, G.Y., Kim, S.P., Jeong, S.W., Park, S.S., 2014. Contrasting development of the latest Quaternary slope failures and mass transport deposits in the Ulleung Basin, East Sea (Japan Sea). In: Krastel, S., Behrmann, J.H., V}olker, D., Stipp, M., Berndt, C., Urgeles, R., Chaytor, J., Huhn, K., Strasser, M., Harbitz, C.B. (Eds.), Submarine Mass Movements and Their Consequences e 6th International Symposium, Advances in Natural and Technological Hazards Research, vol. 37. Springer, pp. 403–412.

Lee, S.H., Jung, W.Y., Bahk, J.J., Gardner, J.M., Kim, K.J., Lee, H.S., 2013. Depositional features of co-genetic turbidite-debrite beds and possible mechanisms for their formation in distal lobated bodies beyond the base-of-slope, Ulleung Basin, East Sea (Japan Sea). Marine Geology 346, 124–140. https://doi.org/10.1016/j.margeo.2013.09.001

Lee, B., Ryang, W.H., Doh, S.J., 2013. Paleomagnetism on the Quaternary marine sediment at the DH-1 long-core site in the Korean continental margin of the East Sea. Geosciences Journal 17 (3), 279–287. https://doi.org/10.1007/s12303-013-0033-z

Lenz, B.L., Sawyer, E.D., 2021. Mass transport deposits in reflection seismic data offshore Oregon, USA. Basin Research 34(1), 81–98.

L'Heureux, J.S., Longva, O., Steiner, A., Hansen, L., Vardy, M.E., Vanneste, M., Haflidason, H., Brendryen, J., Kvalstad, T.J., Forsberg, C.F., and et al., 2012. Identification of weak layers and their role for the stability of slopes at Finneidfjord, northern Norway. In: Submarine Mass Movements and Their Consequences. Y. Yamada, K. Ikehara, Y. Ogawa, R. Urgeles, D. Mosher, J. Chaytor, M. Strasser [Eds], Advances in Natural and Technological Hazards Research, vol. 29, Springer, Dordrecht, The Netherlands, pp. 321–330. https://doi.org/10.1007/978-94-007-2162-3_29

Lim, C., Toyoda, K., Ikehara, K., Peate, D.W., 2013. Late Quaternary tephrostratigraphy of Baegdusan and Ulleung Volcanoes using marine sediments in the Japan Sea/East Sea. Quaternary Research 80, 76–87. https://doi.org/10.1016/j.yqres.2013.04.002

Lisiecki, L.E., and Raymo, M.E., 2005. A Pliocene-Pleistocene stack of 57 globally distributed benthic δ^{18}O records, Paleoceanography 20, PA1003. https://doi.org/10.1029/2004PA001071

Llopart, J., Urgeles, R., Camerlenghi, A., Lucchi, R.G., Rebesco, M., De Mol, B., 2015. Late Quaternary development of the Storfjorden and Kveithola Trough Mouth Fans, northwestern Barents Sea. Quaternary Science Reviews 129, 68–84. https://doi.org/10.1016/j.quascirev.2015.10.002

Locat, L., and Lee, H.J., 2002. Submarine landslides: advances and challenges. Canadian Geotechnical Journal 39, 193–212. https://doi.org/10.1139/t01-089

Locat, J., and Lee, J., 2005. Subaqueous Debris Flows. Chapter 9, In: Mathias et Hungr (Eds.), Debris-flows Hazards and Related Phenomena, Springer, pp. 203–245.

Locat, A., Jostad, H.P., Leroueil, S., 2013. Numerical modeling of progressive failure and its implications for spreads in sensitive clays. Canadian Geotechnical Journal 50(9), 961–978. https://doi.org/10.1139/cgj-2012-0390

Locat, J., Leroueil, S., Locat, A., Lee, H., 2014. Weak layers: their definition and classification from a geotechnical perspective. In Submarine Mass Movements and their Consequences: 6th International Symposium Adv. Nat. Technol. Hazard Res. vol. 37, Krastel, S., Behrmann, J.-H., Völker, D., Stipp, M., Berndt, C., Urgeles, R., Chaytor, J., Huhn, K., Strasser, M., Harbitz, C.B. [Eds.], Springer, Dordrecht, Netherlands, pp. 3–12. https://doi.org/10.1007/978-3-319-00972-8_1

Lykousis, V., Roussakis, G., Sakellariou, D., 2009. Slope failures and stability analysis of shallow water prodeltas in the active margins of Western Greece, northeastern Mediterranean Sea, Int. J. Earth Sci. (Geol Rundsch) 98, 807–822. https://doi.org/10.1007/s00531-008-0329-9

Masson, D.G., Harbitz, C.B., Wynn, R.B., Pedersen, G., Lovholt, F., 2006. Submarine landslides: processes, triggers, and hazard prediction. Philosophical Transactions of the Royal Society A 364, 2009–2039. http://dx.doi.org/10.1098/rsta.2006.1810

Masson, D.G., Wynn, R.B., Talling, P.J., 2010. Large landslides on passive continental margins: Processes, hypotheses and outstanding questions. In: Submarine Mass Movements and Their Consequences, Adv. Nat. Technol. Hazards Res., vol. 28, [Eds.] D.C. Mosher et al., Springer, Doredrecht, Netherlands, pp. 153–165. https://doi.org/10.1007/978-90-481-3071-9_13

McAdoo, B., Watts, P., 2004. Tsunami hazard from submarine landslides on the Oregon continental slope. Marine Geology 203(3–4), 235–245.

Meckler, A.N., Sigman, D.M., Gibson, K.A., François, R., Martínez-García, A., Jaccard, S.L., Röhl, U., Peterson, L.C., Tiedemann, R., Haug, G.H., 2013. Deglacial pulses of deep-ocean silicate into the subtropical North Atlantic Ocean. Nature, 495(7442), 495–498. https://doi.org/10.1038/nature12006

Micallef, A., Masson, D.G., Berndt, C., Stow, D.A.V., 2007. Morphology and mechanics of submarine spreading: a case study from the Storegga Slide. Journal of Geophysical Research 112, F03023. https://doi.org/10.1029/2006JF000739

Moore, Z.T. and D.E., Sawyer, 2016. Assessing post-failure mobility of submarine landslides from seismic geomorphology and physical properties of mass transport deposits: an example from the seaward of the Kumano Basin, Nankai Trough, offshore Japan. Marine Geology 374, 73–84. https://doi.org/10.1016/j.margeo.2016.02.003

Mueller, K., Hough, S., Bilham, R., 2004. Analysing the 1811–1812 New Madrid earthquakes with recent instrumentally recorded aftershocks. Nature 429, 284–288.

Morgenstern, N.R., 1967. Submarine slumping and the initiation of turbidity currents. In: Richards, A.F. (Ed.), Marine geotechnique. University of Illinois Press, Urbana, pp. 189–220.

Morgenstern, N.R., and Price, V.E., 1965. The analysis of the stability of general slip surfaces. Géotechnique 15 (1), 79–93.

Nagashima, K., Tada, R., Matsui, H., Irino, T., Tani, A., Toyoda, S., 2007. Orbital- and millennial-scale variations in Asian dust transport path to the Japan Sea. Palaeogeography, Palaeoclimatology, Palaeoecology, Quaternary Paleoceanography of the Japan Sea and its linkage with Asian Monsoon 247, 144–161. https://doi.org/10.1016/j.palaeo.2006.11.027

Normandeau, A., Campbell, D.C., Piper, D.J.W., Jenner, K., 2019. New evidence for a major late-Quaternary submarine landslide on the external western levee of Laurentian Fan. In: Lintern, D.G. (Ed.), Subaqueous Mass Movements and Their Consequences: Assessing Geohazards, Environmental Implications and Economic Significance of Subaqueous Landslides. Geol. Soc. London, Special Publications 477, pp. https://doi.org/10.1144/SP477.14

Pecher, I.A., Barnes, P.M., LeVay, L.J., and et al., 2018. Creeping Gas Hydrate Slides and Hikurangi. IODP Expedition 372 Preliminary Report 372, Texas A&M University, Texas.

Piper, D.J.W., Shor, A.N., Hughes Clarke, J.E., 1988. The 1929 Grand Banks Earthquake, Slump, and Turbidity Current, In: Clifton, H.E. (Ed.), Sedimentologic Consequences of Convulsive Geologic Events, Special Papers, Geological Society of America 229, 77– 92. https://doi.org/10.1130/SPE229-p77

Piper, D.J.W., Cochonat, P., Morrison, M.L., 1999. The sequence of events around the epicentre of the 1929 Grand Banks earthquake: initiation of debris flows and turbidity currents inferred from sidescan sonar. Sedimentology 46, 79–97. https://doi.org/10.1046/j.1365-3091.1999.00204.x

Piper, D., Mosher, D., Campbell, D., 2012. Controls on the distribution of major types of submarine landslides. In: Clague, J., and Stead, D., (Eds.), Landslides: Types, Mechanisms and Modeling (pp. 95-107). Cambridge: Cambridge University Press. doi:10.1017/CBO9780511740367.010.

Pittenger, A., Taylor, E., and Bryant, W.R., 1989. The influence of biogenic silica on the geotechnical

stratigraphy of the Vøring Plateau, Norwegian Sea, In: Eldholm, O. et al., [Eds.], Proceedings of the Ocean Drilling Program, Scientific Results, Volume 104: College Station, Texas, Ocean Drilling Program, pp. 923–940. https://doi.org/10.2973/odp.proc.sr.104.145.1989

Rack, F.R., Bryant, W.R., Julson, A.P., 1993. Micofabric and physical properties of deep-see high latitude carbonate oozes. In Rezak, R., and Lavoie, D.L., (Eds.,) Carbonate microfabrics. New York, (Springer-verlag), 129–147.

Riedel, M., Cote, M.M., Urlaub, M., Geersen, J., Scholz, N.A., Naegeli, K. and Spence, G.D. 2018. Slope failures along the deformation front of the Cascadia margin: linking slide morphology to subduction zone parameters. Geological Society, London, Special Publications, 477, 47–67, https://doi.org/10.1144/SP477.33.

Ryang, W.-H., Kwon, Y.-K., Kim, S.-P., Kim, D.-C., Choi, J.-H., 2014. Geoacoustic model at the DH-1 long-core site in the Korean continental margin of the East Sea. Geosciences Journal 18(3), 269–279. https://doi.org/10.1007/s12303-014-0005-y

Ryu, B.J., Kim, G.Y., Chun, J.H., Bahk, J.J., Lee, J.Y., Kim, J.-H., Yoo, D.G., Collett, T.S., Riedel, M., Torres, M.E., Lee, S.R., and the UBGH2 Scientists, 2012. Expedition Report of The Second Ulleung Basin Gas Hydrate Drilling Expedition 2 (UBGH2). KIGAM, Daejeon, Korea, pp. 667.

Sawyer, D.E. and Hodelka, B., 2016. Tiny Fossils, Big Impact: The Role of Foraminifera-Enriched Condensed Section in Arresting the Movement of a Large Retrogressive Submarine Landslide in the Gulf of Mexico. Lamarche, G. et al. (Eds.), in Submarine Mass Movements and their Consequences, Advances in Natural and Technological Hazards Research 41, 479–486. https://doi.org/10.1007/978-3-319-20979-1_48

Sawyer, D.E., Flemings, P.B., Dugan, B., Germaine, J.T., 2009. Retrogressive failures recorded in mass transport deposits in the Ursa Basin, Northern Gulf of Mexico. Journal of Geophysical Research 114, B10102. https://doi.org/10.1029/2008JB006159

Sawyer, D.E., Flemings, P.B., Buttles, J., Mohrig, D., 2012. Mudflow transport behavior and deposit morphology: Role of shear stress to yield strength ratio in subaqueous experiments. Marine Geology 307–310, 28–39. https://doi.org/10.1016/j.margeo.2012.01.009

Shiihara, M., Domitsu, H., Torii, M., Nagahashi, Y., Okuno, M., 2013. Stratigraphy and chronology of Holocene tephras from Ulleungdo volcano (South Korea) distributed in and around the Sea of Japan. The Quaternary Research 52, 225–236. https://doi.org/10.4116/jaqua.52.225.

Silva, P.G., Elez, J., Pérez-López, R., Giner-Robles, J.L., Gómez-Diego, P.V., Roquero, E., Rodríguez-Pascua, M.A., Bardají, T., 2021. The AD 1755 Lisbon Earthquake-Tsunami: Seismic source

modelling from the analysis of ESI-07 environmental data. Quaternary International, https://doi.org/10.1016/j.quaint.2021.11.006.

Stow, D.A.V., Reading, H.G., Collinson, J., 1996. Deep seas. In: Sedimentary environments and facies. Blackwell Science Publications, pp. 380–442.

Tada, R., Koizumi, I., Cramp, A., Rahman, A., 1992. Correlation of dark and light layers, and the origin of their cyclicity in the Quaternary sediments from the Japan Sea. Proceedings of ODP Scientific Results 127/128(1), 577–601. https://doi.org/10.1016/10.2973/odp.proc.sr.127128-1.160.1992

Tada, R, Irino, T., Koizumi, I., 1999. Land-ocean linkages over orbital and millennial timescale recorded in Late Quaternary sediments of Japan Sea. Paleoceanography 14, 236–247. https://doi.org/10.1029/1998PA900016

Tada, R., Murray, R.W., Alvarez Zarikian, C.A., and Expedition 346 Scientists, 2015. Proceedings of the Integrated Ocean Drilling Program Volume 346. Integrated Ocean Drilling Program, College Station, TX. https://doi.org/10.2204/iodp.proc.346.2015

Tada, R., Irino, T., Ikehara, K., Karasuda, A., Sugisaki, S., Xuan, C., Sagawa, T., Itaki, T., Kubota, Y., Lu, S., Seki, A., Murray, R.W., Alvarez Zarikian, C.A., Anderson, W.T. Jr., Bassetti, M-A., Brace, B.J., Clemens, S.C., da Costa Gurgel, M.H., Dickens, G.R., Dunlea, A.G., Gallagher, S.J., Giosan, L., Henderson, A.C.G., Holbourn, A.E., Kinsley, C.W., Lee, G.S., Lee, K.E., Lofi, J., Lopes, C.I.C.D., Peterson, L.C., and et al., 2018. High-resolution and high-precision correlation of dark and light layers in the Quaternary hemipelagic sediments of the Japan Sea recovered during IODP expedition 346. Progress in Earth and Planetary Science 5(1) 19, 1–10. https://doi.org/10.1186/s40645-018-0167-8

Takagi, H., Pratama, M.B., Kurobe, S., Esteban, M., Aranguiz, R., Kem B., 2019. Analysis of generation and arrival time of landslide tsunami to Palu City due to the 2018 Sulawesi earthquake. Landslides 16 (5), 983–991.

Tanaka, H., and Locat, J., 1999. A microstructural investigation of Osaka Bay clay: The impact of Microfossils on its mechanical behaviour: Canadian Geotechnical Journal, v. 36, p. 493–508.

Tappin, D.R., Watts, P., McMurtry, G.M., Lafoy, Y., Matsumoto, T., 2002. Prediction of slump generated tsunamis: The July 17th 1998 Papua New Guinea event. Science of Tsunami Hazards, 20(4), 222–238.

ten Brink, U.S., Lee, H.J., Geist, E.L., Twichell., D., 2009. Assessment of tsunami hazard to the US East Coast using relationships between submarine landslides and earthquakes. Marine Geology 264 (1-2), 65–73.

Tiedemann, R., 1991. Acht Millionen Jahre Klimageschichte von Nordwest Afrika und Paläo-ozeanographie des angrenzenden Atlantik: Hochauflösende Zeitreihen von ODP-Sites 658–661, PhD 501 thesis, University of Kiel, 46, 190 pp. https://doi.org/10.2312/reports-gpi.1991.46

Urgeles, R., Bahk, J.-J., Lee, S.-H., Horozal, S., Cukur, D., Kim, S.-P., Kim, G.-Y., Jeong, S.-W., Um, I.-K., 2019. Tsunami hazard from submarine landslides: Scenario-based assessment in the Ulleung Basin, East Sea. Geoscience Journal 23, 439–460. https://doi.org/10.1007/s12303-018-0044-x

Urlaub, M., Geersen, J., Krastel, S., Schwenk, T., 2018. Diatom ooze: Crucial for the generation of submarine mega-slides? Geology 46, 2–5. https://doi.org/10.1130/G39892.1

Watanabe, S., Tada, R., Ikehara, K., Fujine, K., Kido Y., 2007. Sediment fabrics, oxygenation history, and circulation modes of Japan Sea during the Late Quaternary. Palaeogeogr Palaeoclimatol Palaeoecol 247(1–2):50–64. https://doi.org/10.1016/j.palaeo.2006.11.021

Watts, P., 2004. Probabilistic predictions of landslide tsunamis off Southern California. Marine Geology 203 (3-4), 281–301.

Widess, M.B., 1973. How thin is a thin bed, Geophysics 38, 1176 – 1180.

Wiemer, G., Dziadek, R., and Kopf, A., 2017. The enigmatic consolidation of diatomaceous sediment. Marine Geology 385, 173–184. https://doi.org/10.1016/j.margeo.2017.01.006